Annales Societatis Geologorum Poloniae (2024), vol. 94: 297–328 https://doi.org/10.14241/asgp.2024.17

RAMAN MICROSPECTROSCOPY OF MONAZITE-(Ce) AND XENOTIME-(Y): EXAMPLES FROM EXPERIMENTS AND NATURE

Fabian TRAMM [1*], Grzegorz RZEPA [2], Bartosz BUDZYŃ [1], Gabriela A. KOZUB-BUDZYŃ [2], Jakub DYBAŚ [3] & Jiří SLÁMA [4]

[1] *Institute of Geological Sciences, Polish Academy of Sciences, Research Centre in Kraków, Senacka 1, PL 31-002 Kraków, Poland, emails: ndtramm@cyf-kr.edu.pl, ndbudzyn@cyf-kr.edu.pl*
[2] *AGH University of Krakow, Faculty of Geology, Geophysics and Environmental Protection, Mickiewicza 30, 30-059 Kraków, Poland; emails: gprzepa@cyf-kr.edu.pl, lato@agh.edu.pl*
[3] *Jagiellonian University, Jagiellonian Centre for Experimental Therapeutics (JCET), Bobrzyńskiego 14, 30-348 Kraków, Poland; email: jakub.dybas@uj.edu.pl*
[4] *The Czech Academy of Sciences, Institute of Geology, Rozvojová 269, Prague 6 16500, Czech Republic; email: slama@gli.cas.cz*
** Corresponding author*

Tramm, F., Rzepa, G., Budzyń, B., Kozub-Budzyń, G. A., Dybaś, J. & Sláma, J., 2024. Raman microspectroscopy of monazite-(Ce) and xenotime-(Y): examples from experiments and nature. *Annales Societatis Geologorum Poloniae*, 94: 297–328.

Abstract: This work presents an investigation of naturally and experimentally unaltered and altered monazite-(Ce) and xenotime-(Y), as well as secondary phases and synthetic REE phosphates (YPO_4 and $LaPO_4$–$LuPO_4$) with Raman microspectroscopy, using 488 nm, 532 nm, 633 nm and 780 nm excitation lasers, supplemented by electron probe microanalysis (EPMA) and laser ablation inductively coupled plasma mass spectrometry (LA-ICPMS). Monazite-(Ce) spectra of the 532 nm laser from experimental products display a wide range of band positions of the $\nu_1(PO_4)$ symmetric stretching band from 962 to 981 cm^{-1}. Secondary fluorcalciobritholite spectra display a prominent band at 962–965 cm^{-1}, a broader band at ca. 860 cm^{-1} and broad distinct luminescence effects at mid-range. Xenotime-(Y) spectra from experimental products display only minor spectral changes, except for a few spectra near secondary Y-rich fluorcalciobritholite. Spectra of Y-rich fluorcalciobritholite from 532 nm laser display characteristic broad luminescence effects at the range of 1500–3000 cm^{-1}, including a strong luminescence band at ca. 2600 cm^{-1} (Sm^{3+} electronic transition), and are accompanied by a broad band at 974 cm^{-1} (488 nm laser) and 964 cm^{-1} (633 nm laser). The characteristic changes in monazite-(Ce) spectra near secondary phases are emphasised with hyperspectral maps and EPMA-WDS X-ray compositional maps, which provide spatial context and reveal underlying interferences, important to be noted, when evaluating altered minerals. In all cases, experimental and natural, high values of the full width at half maximum (FWHM) of the $\nu_1(PO_4)$ band of unaltered monazite-(Ce) domains represent moderate radiation damage. In contrast, lower FWHM values were observed in altered domains. This work expands the Raman database onto examples of naturally and experimentally altered monazite-(Ce) and xenotime-(Y) enabling the identification of internal structural changes in unaltered and altered domains and differentiation of monazite-(Ce) or xenotime-(Y) from fluorcalciobritholite, Y-rich fluorcalciobritholite and other secondary phases.

Keywords: Monazite-(Ce) stability, fluorcalciobritholite, dissolution-reprecipitation reactions, radiation damage, band narrowing, luminescence effects, hyperspectral mapping.

Manuscript received 13 September 2024, accepted 20 December 2024

INTRODUCTION

Monazite-(Ce), a light rare earth elements (LREE) phosphate, is an accessory mineral that forms in a broad variety of geological environments, such as igneous and metamorphic rocks, and sediments (Williams *et al.,* 2007, 2017; Kylander-Clark, 2017). Xenotime-(Y) (YPO_4) on the other hand, represents the member of the APO_4 series that

is dominated by Y and heavy rare earth elements (HREE) and, though less abundant in Earth's crust than monazite-(Ce), forms in a wide range of rocks, during diagenesis (Rasmussen, 2005; Vallini *et al.,* 2005; Rasmussen *et al.,* 2010; McNaughton and Rasmussen, 2018), igneous processes and low- to high-grade metamorphism (Hawkins and Bowring, 1999; Spear and Pyle, 2002; Broska *et al.,* 2005; Hetherington *et al.,* 2008; Budzyń *et al.,* 2018, 2023a, b; McNaughton and Rasmussen, 2018) and in hydrothermal veins (Vielreicher *et al.,* 2003; Sarma *et al.,* 2011; Fielding *et al.,* 2017; Jian *et al.,* 2024).

Both monazite-(Ce) and xenotime-(Y) are used in U-Th-Pb geochronology (e.g., Harrison *et al.,* 2002; Williams *et al.,* 2007, 2017; Hetherington *et al.,* 2008; Budzyń *et al.,* 2018, 2021; McNaughton and Rasmussen, 2018; Joseph *et al.,* 2021) and as geothermometers (Kingsbury *et al.,* 1993; Gratz and Heinrich, 1997; Heinrich *et al.,* 1997; Andrehs and Heinrich, 1998; Pyle and Spear, 2000; Pyle *et al.,* 2001). Their relevance for geochronology lies (i) in their capability to incorporate significant amounts of Th (particularly in monazite-(Ce)) and U (Förster, 1998; Seydoux-Guillaume *et al.,* 2002b), and (ii) a high closure temperature of ca. 900 °C (Cherniak *et al.,* 2004; Cherniak, 2006, 2010), which limits the diffusion of Pb in monazite-(Ce) and xenotime-(Y) within most geological environments in the Earth's crust. High contents of Th and U lead to self-irradiation in minerals and consequently cause the accumulation of structural damage over time (radiation damage). This process results in metamictisation, which is typical for zircon (Nasdala *et al.,* 1998, 2001; Geisler *et al.,* 2007; Ende *et al.,* 2021), whereas monazite-(Ce) and xenotime-(Y) remain partially crystalline over a long time (Urusov *et al.,* 2012; Nasdala *et al.,* 2018, 2020; Seydoux-Guillaume *et al.,* 2018). This is attributed to structural recovery by the thermal annealing of monazite-(Ce) and xenotime-(Y), which occurs in monazite-(Ce) at temperatures as low as 180 °C (Urusov *et al.,* 2012; Nasdala *et al.,* 2018, 2020; Seydoux-Guillaume *et al.,* 2018).

Alteration of monazite-(Ce) and xenotime-(Y), caused by alkaline fluids or metamorphic reactions, can undermine its stability at a broad range of P-T conditions (Broska and Siman, 1998; Finger *et al.,* 1998; Harlov *et al.,* 2007, 2011; Harlov and Hetherington, 2010; Budzyń *et al.,* 2011, 2015, 2017, 2021; Williams *et al.,* 2011; Harlov and Wirth, 2012; Seydoux-Guillaume *et al.*, 2012; Didier *et al.,* 2013; Ruiz-Agudo *et al.,* 2014; Grand'Homme *et al.,* 2016, 2018; Macdonald *et al.,* 2017). The dominant factors that sustain fluid-induced alteration are coupled dissolution-reprecipitation processes due to the formation of interconnected microporosity, providing fluid pathways and partial or complete replacement of monazite-(Ce) or xenotime-(Y) by secondary phases and may result in significant element transport (Putnis, 2002, 2009; Harlov *et al.,* 2007, 2011; Budzyń *et al.,* 2010, 2011, 2015, 2017, 2021; Hetherington *et al.,* 2010; Putnis and Austrheim, 2010, 2013; Williams *et al.,* 2011; Seydoux-Guillaume *et al.,* 2012; Didier *et al.,* 2013; Ruiz-Agudo *et al.,* 2014; Grand'Homme *et al.,* 2016).

This study provides new insights to the characterisation of monazite-(Ce) and xenotime-(Y) using Raman microspectroscopy with various lasers (488 nm, 532 nm, 633 nm and 780 nm) and two different instruments. Evaluation of Raman spectra includes primary Raman features and characteristic luminescence effects, caused by rare earth elements (REE). The investigations involved (i) monazite-(Ce) and xenotime-(Y) from experimental products from fluid-mediated alteration caused by Ca- and Na-rich fluids across wide range of P-T conditions, (ii) naturally altered monazite-(Ce) from Ankazobe (Madagascar), (iii) xenotime-(Y) from a pegmatite from Piława Górna (Poland) and, for comparison, (iv) synthetic end-members of REE phosphates ($LaPO_4$–$LuPO_4$ and YPO_4). This work demonstrates characteristic changes in monazite-(Ce) and xenotime-(Y) spectra, such as band narrowing or broadening, the appearance of additional bands and the rise of luminescence effects. The additional Raman data on monazite-(Ce), xenotime-(Y), and secondary fluorcalciobritholite may serve as a reference for future investigations of monazite-(Ce) and xenotime-(Y). Implications drawn in this work highlight the importance of Raman microspectroscopy on monazite-(Ce) and xenotime-(Y) used in petrochronology to gain structural information without affecting the mineral itself before isotopic U-(Th-)Pb measurements.

BACKGROUND ON RAMAN MICROSPECTROSCOPY OF MONAZITE-(Ce) AND XENOTIME-(Y)

Raman microspectroscopy of natural monazite-(Ce) (e.g., Seydoux-Guillaume *et al.,* 2002c, 2018; Lenz *et al.,* 2015) and comparison with Raman data of synthetic orthophosphates (e.g., Begun *et al.,* 1981; Silva *et al.,* 2006; Heuser *et al.,* 2014; Clavier *et al.,* 2018; Lalla *et al.,* 2021) can provide important information about the vibrational contribution of REE. Vibrational features of the monazite-(Ce) structure are defined by factor group analysis ($\Gamma_T = 18A_g + 17A_u + 18B_g + 16B_u$; Begun *et al.,* 1981). Thirty-six of those vibrational modes are Raman-active (i.e., $\Gamma_{int} = 9A_g + 9B_g$, $\Gamma_{ext} = 9A_g + 9B_g$; Begun *et al.,* 1981). These Raman-active modes are based on the monoclinic structure of monazite-(Ce) ($P2_1/n$ (Z = 4) space group symmetry), in which the PO_4 tetrahedra are interconnected with the polyhedral structures in a ninefold oxygen coordination (Clavier *et al.,* 2011; Lalla *et al.,* 2021). The polyhedral structure is arranged as monodentate tetrahedra with a pentagon of five oxygens on the equatorial plane. This structure is interpenetrated by a tetrahedron of four oxygen atoms, which belongs to two bidentate tetrahedra (Ni *et al.,* 1995; Clavier *et al.,* 2011; Lalla *et al.,* 2021). Raman spectra of monazite-(Ce) typically result in lattice modes ranging from 100 to 350 cm^{-1}, internal PO_4 bending modes ranging from 500 to 700 cm^{-1}, and the most dominant symmetric stretching mode $\nu_1(PO_4)$ in the range of ca. 960 to 990 cm^{-1} (Geisler *et al.,* 2016). These represent the primary Raman features of the monazite-(Ce) spectrum.

Xenotime-(Y) is a tetragonal mineral, which is isostructural to zircon in a space group of D_{4h}^{19} ($I4_1/amd$), Z = 2 (Wyckoff, 1965; Begun *et al.,* 1981; Ni *et al.,* 1995; Mullica *et al.,* 1996; Boatner, 2002; Huminicki and Hawthorne, 2002). The xenotime-(Y) structure contains twelve Raman

active modes (i.e., $\Gamma_{ext} = 2B_{1g} + 3E_g : \Gamma_{int} = 2A_{1g} + 2B_{1g} + B_{2g} + 2E_g$; Begun *et al.,* 1981). The Raman spectrum of xenotime-(Y) can be divided, like spectra of monazite-(Ce), into primary Raman features that are lattice modes (ca. 100–300 cm^{-1}), internal (PO_4) bending modes (ca. 500–700 cm^{-1}) and $\nu_1(PO_4)$ symmetric stretching modes (ca. 900–1000 cm^{-1}).

Luminescence effects are common in Raman microspectroscopy and can be recognised by comparison of spectra using multiple laser wavelengths. If bands are shifting positions, disappear, or new bands appear with different lasers, they are most likely caused by luminescence. Luminescence effects commonly show broad background bands that can completely superimpose Raman signals. However, luminescence effects caused by REE appear as relatively sharp and characteristic bands, because of the unique electronic configuration of the 4*f* orbital (e.g., Dieke and Crosswhite, 1963; Lenz *et al.,* 2013, 2015; Gaft *et al.,* 2015).

MATERIALS AND METHODS

Materials

Synthetic REE phosphates (YPO_4, $LaPO_4$–$LuPO_4$), used in the Laboratory of Critical Elements AGH-KGHM (the Faculty of Geology, Geophysics and Environmental Protection, AGH University of Krakow) as reference materials for EPMA measurements were analysed with Raman microspectroscopy to compare spectra of high purity end-members with those of monazite-(Ce) and xenotime-(Y) from experimental products and natural examples. The crystals are up to several mm in size and embedded in a polished 1" grain mount.

Monazite-(Ce) and xenotime-(Y) from various materials with different concentrations of REE, U, Th, different ages and different degrees of alteration were investigated in this work. This includes monazite-(Ce) and xenotime-(Y) from (i) products of laboratory experiments focused on the stability of monazite-(Ce) and xenotime-(Y) (Budzyń and Kozub-Budzyń, 2015; Budzyń *et al.,* 2015, 2017), (ii) altered monazite-(Ce) from Ankazobe (Madagascar), and (iii) altered xenotime-(Y) from Piława Górna in the Góry Sowie Block, SW Poland (Budzyń *et al.,* 2018; Tramm *et al.,* 2021).

Monazite-(Ce) and xenotime-(Y) grains were selected from products of five experiments performed utilising cold-seal autoclaves on a hydrothermal line under P-T conditions of 200 MPa / 350 °C, 400 MPa / 450 °C, and the piston-cylinder apparatus under P-T conditions of 600 MPa / 550 °C, 800 MPa / 650 °C, and 1000 MPa / 750 °C (Tabs 1, 2) at the GeoForschungsZentrum Potsdam (Germany). The Burnet monazite-(Ce) and NWFP xenotime-(Y) used in experiments were also selected for analysis. Starting materials for experiments with monazite-(Ce) included natural pegmatitic monazite-(Ce) from Burnet County, Texas, USA (Burnet monazite-(Ce); age 1100.5 ± 1.1.6 Ma, Budzyń *et al.,* 2021), albite, sanidine, biotite, muscovite, SiO_2, CaF_2, $Na_2Si_2O_5$ and doubly distilled H_2O. Starting materials in the experiments with xenotime-(Y) included xenotime-(Y) from the North-West Frontier Province in Pakistan (NWFP xenotime-(Y); 38.4 ± 0.6 Ma, Budzyń and Sláma, 2019), albite, labradorite, sanidine, biotite, muscovite, garnet, SiO_2, CaF_2, $Na_2Si_2O_5$ and doubly distilled H_2O. For more details on experimental procedures see previous works (Budzyń and Kozub-Budzyń, 2015; Budzyń *et al.,* 2015, 2017).

The experimental products with monazite-(Ce) and xenotime-(Y) were embedded in epoxy. Polished 1" grain mounts were initially investigated with backscattered electron (BSE) imaging and energy dispersive spectroscopy (EDS) analysis without carbon coating using a field emission scanning electron microscope FEI Quanta 200 under a low-vacuum at the Faculty of Geology, Geophysics and Environmental Protection, AGH University of Krakow.

A piece of a fist-size crystal (ca. 278 g) of monazite-(Ce) from Ankazobe, Madagascar (henceforth, Ankazobe monazite-(Ce)) was embedded in a 1" epoxy mount and polished. The Ankazobe monazite-(Ce) (515.4 ± 4.8 Ma, MSWD = 0.90, LA-ICPMS U-Pb analysis; Budzyń and Sláma – unpublished data) was supplied by a mineral dealer. The studied crystal has finely porous domains and a narrow altered "rim" that contains xenotime-(Y), mica and Th-silicat.

A natural example of altered xenotime-(Y) is a large crystal, intergrown with zircon in a pegmatite from Piława Górna (Budzyń *et al.,* 2018; Tramm *et al.,* 2021). The xenotime-(Y) (PG xenotime-(Y), henceforth) crystallised in a Palaeoproterozoic pegmatite (ca. 2.09 Ga) and was incorporated into a newly formed Devonian pegmatite (ca. 370 Ma; Budzyń *et al.,* 2018). The xenotime-(Y), investigated in a thin section of the pegmatite, is patchy-zoned in high-contrast backscattered electron (BSE) imaging and contains domains with extensive microporosity partially filled with secondary phases. The xenotime-(Y) demonstrates a patchy zoned domain ("outer" domain) and a domain with extensive microporosity close to the phase boundary with zircon (Budzyń *et al.*, 2018; Tramm *et al.*, 2021).

Analytical procedure

Raman microspectroscopy

Synthetic REE phosphates ($LaPO_4$–$LuPO_4$) were analysed with two excitation lasers of 532 nm and 780 nm to distinguish primary Raman features from luminescence effects. Raman microspectroscopy measurements of the monazite-(Ce) and xenotime-(Y) from experimental products, the Ankazobe monazite-(Ce) and the PG xenotime-(Y) were predominantly conducted with the 532 nm laser excitation. These Raman spectroscopic investigations were done using a Thermo Scientific DXR Raman Microscope (henceforth, instrument A) at the Faculty of Geology, Geophysics and Environmental Protection, AGH University of Krakow. Measurements involving the 532 nm excitation laser were performed at room temperature using an apparatus of a 25 μm pinhole, a 900 lines / mm grating, a CCD detector, and an air Olympus (100× / 0.80 NA) objective. Single spot measurements were conducted at 10 mW, an exposure time of 3 s, and 100 accumulations. Measurements with the 780 nm excitation laser were performed at 15 mW power, exposure time of 3 s, 100 accumulations and a grating of 400 lines / mm. All displayed Raman spectra collected with instrument A range from 150 to 3500 cm^{-1} to avoid artefacts below 150 cm^{-1}. The spectra were processed using Thermo Scientific OMNIC software. Post-processing of the spectra

Table 1

Summary of experimental conditions and notes on the experimental products from which monazite-(Ce) was selected for Raman microspectroscopy investigations in this study (modified from Budzyń *et al*., 2015, 2017).

Experiment	T (°C)	P (MPa)	Duration (days)	Notes
Exp1	350	200	40	Monazite-(Ce) grains display dissolution pits and porosity at the rim. REE-rich steacyite formed at the surface of monazite-(Ce).
Exp2	450	400	18	Monazite-(Ce) grains are partially replaced by REE-rich steacyite and show dissolution pits along the rim. REE-rich steacyite formed accumulations of crystals at the rim of monazite-(Ce) and fills cracks in monazite-(Ce). Occasionally, small crystals of fluorcalciobritholite formed close to steacyite.
Exp3	550	600	8	Monazite-(Ce) grains display porosity. One grain displays patchy zoning. At the rim of altered monazite-(Ce), REE-rich fluorcalciobritholite formed small crystals. Occasionally, fine crystals of cheralite formed between fluorcalciobritholite and monazite-(Ce).
Exp4	650	800	6	Monazite-(Ce) grains display porosity and dissolution pits at the rim, where fluorcalciobritholite formed. Occasionally fine crystals of cheralite formed between fluorcalciobritholite and monazite-(Ce).
Exp5	750	1000	4	Monazite-(Ce) grains are surrounded by a fine rim of fluorcalciobritholite. A cluster of monazite-(Ce) grains is embedded in melt and partially replaced by fluorcalciobritholite.

Table 2

Summary of experimental conditions and notes on the experimental products from which xenotime-(Y) was selected for Raman microspectroscopy investigations in this study (modified from Budzyń and Kozub-Budzyń, 2015; Budzyń *et al.*, 2017).

Experiment	T (°C)	P (MPa)	Duration (days)	Notes
Exp1	350	200	40	Xenotime-(Y) grains are unaltered and there are no secondary phases on their surface. Minor amounts of tiny crystals of Y-rich silicate, Y-rich apatite and amphibole formed in this run.
Exp2	450	400	18	Xenotime-(Y) grains appear unaltered without the presence of secondary phases on its surface. Secondary phases formed delicate crystals composed of Y-rich silicate, Y-rich apatite and amphibole.
Exp3	550	600	8	Xenotime-(Y) grains appear unaltered without the presence of secondary phases on its surface. Secondary phases formed delicate crystals composed of Y-rich silicate, Y-rich apatite and amphibole.
Exp4	650	800	6	Xenotime-(Y) grains display dissolution pits on the surface. Y-rich fluorcalciobritholite partially replaced xenotime-(Y) or formed on the surface of xenotime-(Y).
Exp5	750	1000	4	Xenotime-(Y) grains display dissolution pits on the surface. Y-rich fluorcalciobritholite partially replaced xenotime-(Y) or formed on the surface of xenotime-(Y). A cluster of xenotime-(Y) grains is embedded in melt and partially replaced by Y-rich fluorcalciobritholite.

was done using luminescence corrections and automatic baseline correction. Deconvolution was done using the Gaussian-Lorentzian band shape after Ruschel *et al.* (2012). Obtained FWHM (full width at half maximum) values of the $v_1(PO_4)$ symmetric stretching band were corrected according to the instrumental broadening (Dijkman and van der Maas, 1976; Irmer, 1985; Nasdala *et al.,* 2001).

Additional investigations were done on selected grains of monazite-(Ce) and xenotime-(Y) from experimental products conducted at the highest and lowest P-T conditions (350 °C / 200 MPa and 750 °C / 1000 MPa, Tabs 1, 2) for comparative spectroscopic evaluations using various excitation lasers (488 nm, 532 nm and 633 nm) and hyperspectral mapping (532 nm and 633 nm). The measurements

were conducted with a WITec confocal CRM alpha 300 Raman microscope (WITec GMBH, Ulm, Germany; henceforth instrument B) at the Raman Imaging Group of the Jagiellonian University (Kraków, Poland). Measurements were performed at room temperature. The spectrometer was equipped with air-cooled solid-state lasers operating at 488 nm, 532 nm and 633 nm, and a Charge Coupled Device (CCD) detector cooled to -60 °C. The excitation lasers were coupled to the microscope via optical fibre with a diameter of 50 μm (488 nm and 532 nm) or 100 μm (633 nm). An air Olympus MPLAN (100× / 0.90 NA) objective was used. The monochromator of the spectrometer was adjusted using a radiation spectrum from a calibrated xenon lamp (WITec UV light source). The standard alignment procedure (single-point calibration) was performed before measurements using the Raman scattering line produced by a silicon plate (520.5 cm^{-1}). The integration time for a single spectrum was 1 s, the number of accumulations per collected spectrum was equal to 100 (acquisition time per single spectrum 100 s), and a spectral resolution equal to 3 cm^{-1} was achieved. Hyperspectral maps were collected with a 0.5 s integration time and a step size of 1 μm. The Raman measurements and data analysis were performed with WITec software (WITec Project Plus 5.1).

Raman microspectroscopy measurements were performed on the samples without carbon-coating, which has been applied later for xenotime-(Y) compositional analysis and BSE imaging with electron probe microanalysis (EPMA). Trace element analyses were conducted, after removal of carbon-coating, with laser ablation inductively coupled plasma mass spectrometry (LA-ICPMS). The EPMA and LA-ICPMS compositional measurements were conducted closely to Raman spots.

Electron probe microanalysis

The EPMA measurements were conducted with a JEOL SuperProbe JXA-8230 electron microprobe equipped with five wavelength dispersive spectrometers (WDS) at the Laboratory of Critical Elements AGH-KGHM at the AGH University of Krakow. Analytical conditions included an acceleration voltage of 15 kV, a beam current of 100 nA and a spot size of 3 μm (see Supplementary Tab. S1 for more details). Data correction was done using an in-house ZAF procedure.

Laser ablation – inductively coupled plasma mass spectrometry

Trace element analyses were conducted using a Thermo Scientific Element 2 high-resolution sector field ICPMS coupled to a 193 nm ArF excimer laser (Teledyne Cetac Analyte Excite laser) at the Institute of Geology of the Czech Academy of Sciences (Prague, Czech Republic). The time-resolved signal data were processed using Glitter software (van Achterbergh *et al.,* 2001). The precision of the analyses (1 RSD) ranges between 5 and 15% for most elements and accuracy was monitored by using a homogenized basalt reference material BCR-2 (USGS). See Supplementary Table S2 for more analytical details.

RESULTS

Raman microspectroscopy of synthetic REE phosphates (YPO_4, $LaPO_4$–$LuPO_4$) – instrument A (532 nm and 780 nm lasers)

The Raman spectra of endmember REE-phosphates (YPO_4, $LaPO_4$–$LuPO_4$) display typical primary Raman features with an increasing spectral position of the symmetric stretching band $v_1(PO_4)$ from 965 cm^{-1} ($LaPO_4$) to 985 cm^{-1} ($GdPO_4$) and a jump to 992 cm^{-1} ($TbPO_4$) to 1009 cm^{-1} ($LuPO_4$) in accordance to the decrease of ionic radii with Z number of REE (Fig. 1; Tabs 3, 4; cf. Begun *et al.,* 1981). Some REE phosphates resonate to the 532 nm with luminescence effects at mid-range (ca. 1400–2700 cm^{-1}), such are $NdPO_4$ ($^2G_{7/2} \rightarrow {}^5I_{9/2}$ electronic transition), $SmPO_4$ ($^4G_{5/2} \rightarrow {}^5H_{7/2}$), $EuPO_4$ ($^5D_0 \rightarrow {}^7F_2$) with luminescence effects that completely superimpose primary Raman features, and low-intensity luminescence effects of $GdPO_4$ and $LuPO_4$ (Fig. 1). Strong luminescence effects superimpose lattice and bending modes at low-range (< 800 cm^{-1}) in $HoPO_4$ and $ErPO_4$ spectra ($^5S_2 \rightarrow {}^5I_8$ and $^4S_{3/2} \rightarrow {}^4I_{15/2}$ electronic transitions). However, primary Raman bands of the symmetric stretching $v_1(PO_4)$ and antisymmetric stretching $v_3(PO_4)$ are still distinguishable. Furthermore, the spectra of $SmPO_4$ display weak and $HoPO_4$ strong luminescence effects at high-range (> 3000 cm^{-1}) contributed by Sm^{3+} ($^4G_{5/2} \rightarrow {}^6H_{9/2}$) and Ho^{3+} ($^5F_5 \rightarrow {}^5I_8$) electronic transitions.

Electronic transitions of luminescence effects are derived from energy levels of Dieke diagrams (Dieke and Crosswhite, 1963). A more convenient display of spectral positions for luminescence effects is the unshifted absolute spectral position (cm^{-1}), which is independent of the laser line and serves as a better indication for other works including luminescence data (the top axis in Figs 1, 2, 8). However, because luminescence effects are compared to primary Raman features (commonly displayed in Raman shift) of monazite-(Ce) and xenotime-(Y) in this work, all given values remain in Raman shift (cm^{-1}) for clarity. Raman microspectroscopy of Burnet monazite-(Ce) and monazite-(Ce) from experimental products (Exp1–Exp5) – Instrument A (532 nm laser).

Raman microspectroscopy of Burnet monazite-(Ce) and monazite-(Ce) from experimental products (Exp1–Exp5) – Instrument A (532 nm laser)

Raman spectra of the Burnet monazite-(Ce) (532 nm) display primary Raman features of (i) lattice modes (150–300 cm^{-1}), (ii) internal bending modes (500–700 cm^{-1}) with a dominant symmetric bending band $v_2(PO_4)$ at 464 cm^{-1}, (iii) a predominant symmetric stretching band $v_1(PO_4)$ at 973 cm^{-1} and (iv) the antisymmetric stretching band $v_3(PO_4)$ at 1067 cm^{-1} (Fig. 2A; Tab. 5). The Burnet monazite-(Ce) spectrum contains luminescence effects caused by electronic transitions of Nd^{3+} ($^2G_{7/2} \rightarrow {}^5I_{9/2}$) and Sm^{3+} ($^4G_{5/2} \rightarrow {}^5H_{7/2}$) ions that are present at mid-range 1500–2500 cm^{-1} and Sm^{3+} ($^4G_{5/2} \rightarrow {}^6H_{9/2}$) at high-range 3000–3500 cm^{-1}. The luminescence effects at mid-range include two broad shoulders and a dominant band at 2029 cm^{-1}.

Table 3

Raman data of synthetic $LaPO_4$–$GdPO_4$ obtained with 532 nm and 780 nm lasers.

532 nm[1]							**780 nm**[1]							**Assigned bands**[2]	
$LaPO_4$	$CePO_4$	$PrPO_4$	$NdPO_4$	$SmPO_4$	$EuPO_4$[3]	$GdPO_4$	$LaPO_4$[3]	$CePO_4$[3]	$PrPO_4$	$NdPO_4$[3]	$SmPO_4$	$EuPO_4$	$GdPO_4$	symmetry	modes
(w) 167	–	**(w) 176**	–	–	–	–	–	–	–	–	–	**(w) 174**	–	Bg	**lattice**
(w) 216	**(w) 217**	–	–	–	–	–	–	–	–	–	–	–	–	Ag,Bg	**lattice**
(w) 223	**(w) 225**	**(w) 221**	–	**(w) 228**	–	**(w) 235**	–	–	–	–	–	–	–	Ag,Bg	**lattice**
–	–	**(w) 230**	**(w) 224**	**(w) 240**	–	–	–	–	**(w) 224**	–	**(m) 230**	**(w) 234**	**(w) 235**	Ag,Bg	**lattice**
(w) 270	–	–	**(w) 234**	–	–	–	–	–	**(w) 233**	–	–	**(s) 244**	**(w) 247**	Ag,Bg	**lattice**
–	–	–	l(w) 281	–	–	–		–	–	–	–	–	–	–	–
–	–	–	–	–	–	–	–	–	–	–	–	–	**(w) 392**	–	–
(w) 393	**(w) 395**	**(w) 395**	–	–	–	**(w) 402**	–	–	**(w) 398**	–	–	**(w) 403**	**(w) 403**	Ag,Bg	**lattice**
(w) 411	–	**(w) 414**	**(w) 416**	**(w) 400**	–	**(w) 425**	–	–	**(w) 417**	–	–	**(w) 425**	–	Ag,Bg	**lattice**
(w) 463	**(w) 465**	**(w) 466**	**(m) 468**	**(w) 470**	–	**(w) 475**	–	–	**(w) 469**	–	**(m) 472**	–	**(m) 476**	Ag,Bg	**$\nu_2(PO_4)$**
(w) 569	–	–	–		–	**(w) 575**	–	–	–	–	–	–	–	–	–
(w) 616	**(w) 618**	**(w) 619**	**(w) 621**	**(w) 625**	–	–	–	–	–	–	**(w) 627**	**(w) 630**	**(w) 632**	Ag,Bg	**$\nu_4(PO_4)$**
–	–	–	–	**(w) 949**	–	–	–	–	–	–	–	–	–	–	–
(s) 965	**(s) 968**	**(s) 971**	**(s) 974**	**(s) 979**	**–**	**(s) 985**	–	**–**	**(s) 974**	**–**	**(s) 981**	**(s) 989**	**(s) 987**	Ag,Bg	**$\nu_1(PO_4)$**
(w) 989	**(w) 990**	**(w) 991**	**(w) 994**	**(w) 996**	–	–	–	–	**(w) 994**	–	**(w) 999**	–	–	–	–
(m) 1054	–	**(m) 1056**	**(w) 1059**	–	–	**(m) 1070**	–	–	**(m) 1058**	–	–	**(m) 1069**	–	–	**$\nu_3(PO_4)$**
(w) 1062	–	–	–	–	–	–	–	–	–	–	–	–	–	–	–
(w) 1072	**(w) 1071**	**(w) 1073**	–	–	–	**(w) 1090**	–	–	**(w) 1076**	–	–	**(w) 1093**	–	–	–

Notes:

[1] – data collected with instrument A;

[2] – assigned bands according to Begun *et al.* (1981) and Silva *et al.* (2006);

[3] – overwhelming luminescence effects prevented unambiguous data deconvolution.

In bold – Raman bands; l – luminescence bands; sh – shoulder. Intensities of presented data are normalized to $\nu_1(PO_4)$ band equal to 1.0: weak (w) 0.05–0.2, medium (m) 0.2–0.5, strong (s) 0.5–1.0. Only significant signals above background are presented.

Table 4

Raman data of synthetic YPO_4 and $TbPO_4$–$LuPO_4$ obtained with 532 nm and 780 nm lasers.

532 nm(1)							
YPO_4	$TbPO_4$	$DyPO_4$	$HoPO_4$	$ErPO_4$	$TmPO_4$	$YbPO_4$	$LuPO_4$
–	–	**(w) 128**	–	–	–	–	–
–	**(w) 138**	**(w) 138**	–	–	**(w) 136**	–	–
–	–	–	l(vs) 167	–	–	–	–
(w) 182	–	–	–	–	–	–	–
–	–	–	l(vs) 232	–	–	–	–
–	–	–	l(vs) 252	–	–	–	–
(w) 296	**(w) 289**	**(m) 293**	l(vs) 290	–	**(w) 301**	–	**(w) 303**
(w) 329	**(w) 329**	–	l(vs) 316	–	**(w) 327**	–	–
–	–	–	l(vs) 362	l(vs)377	–	–	–
–	–	–	l(vs) 404	l(vs)410	–	–	–
–	–	–	l(vs) 418	l(vs)424	–	–	–
–	–	–	l(vs) 436	–	–	–	–
–	–	–	l,sh(vs) 445	l(vs)458	–	–	–
–	–	–	l(vs) 468	–	–	–	–
(w) 481	**(w) 482**	**(w) 483**	l(vs) 494	l(vs)477	**(w) 486**	**(w) 487**	**(w) 486**
–	–	–	l(vs) 503	–	–	–	–
–	–	–	l(vs) 521	l(vs)523	–	–	–
–	–	–	l(vs) 554	–	–	–	–
–	–	**(w) 574**	l(vs) 577	l(vs)571	–	–	**(w) 581**
–	–	–	l(vs) 593	–	–	–	–
–	–	–	l(vs) 624	l(vs)611	–	–	–
–	**(w) 649**	**(w) 651**	l(vs) 645	l(vs)666	**(w) 658**	**(w) 660**	–
–	–	–	–	–	–	–	–
–	**(w) 813**	–	–	–	–	–	–
(s) 999	**(s) 993**	**(s) 995**	**(s) 999**	**(s)1001**	**(s) 1003**	**(s) 1006**	**(s) 1009**
–	–	–	–	–	**sh(w) 1008**	–	–
(w) 1024	**–**	**(w) 1016**	**(w) 1019**	**(w)1021**		**(w) 1027**	**(w) 1030**
(s) 1056	**(s) 1048**	**(m) 1052**	**(s) 1055**	**(m)1058**	**(s) 1061**	**(s) 1065**	**(m) 1067**
mid–range luminescence effects							
–	–	–	–	–	–	–	–
–	–	–	–	–	–	–	–
–	–	–	–	–	–	–	l(w) 1948
–	–	–	–	–	–	–	l(w) 2013
–	–	–	–	–	–	–	–
–	–	–	–	–	–	–	–
–	–	–	–	–	–	–	–
–	–	–	–	–	–	–	–
–	–	–	–	–	–	–	–
high–range luminescence effects							
–	–	–	l(vs) 3234	–	–	–	–
–	–	–	l(vs) 3257	–	–	–	–
–	–	–	l(vs) 3306	–	–	–	–
–	–	–	l(vs) 3327	–	–	–	–
–	–	–	l(vs) 3345	–	–	–	–
–	–	–	l(vs) 3414	l(vs) 3425	–	–	–
–	–	–	l(vs) 3438	l(vs) 3467	–	–	–
–	–	–	l(vs) 3482	–	–	–	–

780 nm[1]								Assigned bands[2]	
YPO_4	$TbPO_4$	$DyPO_4$	$HoPO_4$	$ErPO_4$	$TmPO_4$	$YbPO_4$	$LuPO_4$	symmetry	#
–	–	**(w) 131**	**(w) 131**	**(w) 131**	–	–	–	**Bg**	**22B**
–	**(w) 140**	–	**(w) 139**	**(w) 139**	–	–	**(w) 139**	**Eg**	**21B**
(w) 156	–	–	–	–	l(vs) 149	–	–	–	–
(w) 185	–	–	–	–	l(vs) 182	l(w) 182	**(w) 185**	**Bg**	**18B**
–	–	–	–	–	–	–	–	–	–
–	–	–	–	–	l(vs) 263	l(m) 263	**(w) 267**	**Eg**	**15B**
(m) 299	**(w) 291**	**(m) 294**	**(m) 297**	**(m) 299**	l(vs) 309	l(w) 303	**(m) 304**	**Eg**	**14B**
(w) 331	**(w) 331**	–	**(w) 329**	**(w) 321**	l(vs) 343	l(w) 345	–	**Bg**	**13B**
–	–	–	–	**(w) 384**	l(vs) 388	–	–	–	–
–	–	–	–	–	–	**(w) 406**		–	–
–	–	–	–	–	–	–	–	–	–
–	–	–	–	–	–	–	–	–	–
–	–	–	–	**(w) 440**	l(vs) 456	–	–	–	–
–	–	–	–	–	–	–	–	–	–
(w) 484	**(w) 484**	**(w) 485**	**(w) 485**	**(w) 486**	–	**(w) 489**	**(w) 488**	**Ag**	**10B**
–	–	**sh(w) 507**	–	–	–	–	–	–	–
–	–	–	–	–	–	–	–	–	–
–	–	–	–	–	l(vs) 531	–	–	–	–
(w) 581	–	**(w) 576**	**(w) 577**	**(w) 579**	l(vs) 576	**(w) 581**	**(w) 581**	**Eg**	**8B**
–	–	–	–	–	–	–	–	–	–
–	–	–	–	–	–	–	–	–	–
(w) 659	**(w) 650**	**(w) 652**	–	**(w) 657**	–	–	**(w) 664**	**Bg**	**6B**
–	–	–	–	**(w) 679**	–	–	–	–	–
–	–	–	–	–	–	–	–	–	–
(s) 1001	**(s) 994**	**(s) 997**	**(s) 1000**	**(s) 1002**	**(s) 1005**	**(s) 1007**	**(s) 1010**	**Ag**	**1B**
–	–	–	–	–	–	–	–	–	–
(w) 1026		**(w) 1017**	**(w) 1020**	**(w) 1023**	**(w) 1026**	**(w) 1028**	**(w) 1031**	**Eg**	**2B**
(s) 1058	**(s) 1049**	**(s) 1053**	**(s) 1056**	**(s) 1059**	**(s) 1063**	**(s) 1066**	**(s) 1068**	**Bg**	**3B**
mid–range luminescence effects									
–	–	–	–	–	–	–	–	–	–
–	–	–	–	–	–	–	–	–	–
–	–	–	–	–	–	–	–	–	–
–	–	–	–	–	–	–	–	–	–
–	–	–	–	–	–	–	–	–	–
–	–	–	–	–	–	–	–	–	–
–	–	–	–	–	–	–	–	–	–
–	–	–	–	–	–	–	–	–	–
–	–	–	–	–	–	–	–	–	–
high–range luminescence effects									
–	–	–	–	–	–	–	–	–	–
–	–	–	–	–	–	–	–	–	–
–	–	–	–	–	–	–	–	–	–
–	–	–	–	–	–	–	–	–	–
–	–	–	–	–	–	–	–	–	–
–	–	–	–	–	–	–	–	–	–
–	–	–	–	–	–	–	–	–	–
–	–	–	–	–	–	–	–	–	–

Notes:

[1] – data collected with instrument A;

[2] – assigned bands according to Begun et al. (1981).

In bold – Raman bands; l – luminescence bands; sh – shoulder. Intensities of presented data are normalized to $\nu_1(PO_4)$ band (1B) equal to 1.0: weak (w) 0.05–0.2, medium (m) 0.2–0.5, strong (s) 0.5–1.0, very strong (vs) > 1.0. Only significant signals above background are presented.

Table 5

Raman data of Burnet monazite-(Ce) and monazite-(Ce) from experiments obtained with 532 nm laser.

	Raman spectra and corresponding Raman spots of monazite[1]														**Assigned bands[2]**	
Burnet monazite–(Ce)	Exp1			Exp2			Exp3		Exp4			Exp5			symme-try	modes
	spectrum 1 (n = 8)	spectrum 2 (n = 13)	spectrum 3 (n = 6)	spectrum 4 (n = 11)	spectrum 5 (n = 6)	spectrum 6 (n = 3)	spectrum 7 (n = 7)	spectrum 8 (n = 4)	spectrum 9 (n=4)	spectrum 10 (n=8)	spectrum 11 (n=5)	spectrum 12 n=17)	spectrum 13 (n=7)	spectrum 14 (n=7)		
(n = 6)	spots: 1–6, 8, 9	spots: 11–15, 21–28	spots: 10, 26–20	spots: 29–32, 35–37, 40–43	spots: 33, 34, 38, 39, 44, 45	spots: 47–49	spots: 56–61, 65	spots: 53–55, 64	spots: 66–68, 72	spots: 71, 73–78, 83	spots: 79–81, 84, 85	spots: 86–93, 95–97, 100, 102, 116–118, 120	spots: 103–108, 113	spots: 123–126, 128, 129		
	(w) 163	–	–	–	–	–	**–**	**–**	–	–	–	–	–	–	Bg	**lattice**
–	–	**(w) 180**	**(w) 179**	–	–	**(w) 171**	**–**	**–**	–	–	–	**(w) 184**	–	**(w) 176**	Bg	**lattice**
–	–	–	–	–	**(w) 216**	**(w) 217**	–	–	–	–	–	–	–	–	Ag,Bg	**lattice**
–	**(w) 230**	**(w) 231**	**(w) 232**	**(w) 220**	**(w) 226**	–	**(w) 224**	**–**	–	**(w) 227**	–	**(w) 233**	**(w) 227**	**(w) 222**	Ag,Bg	**lattice**
(w) 225	–	–	–	–	–	–	–	**–**	–	–	–	–	–	–	Ag,Bg	**lattice**
(w) 274	–	–	–	–	–	**(w) 276**	**(w) 280**	**–**	–	–	–	**(w) 289**	–	**(w) 281**	Ag	**lattice**
sh(w) 403	–	**(w) 402**	**(m) 402**	**(w) 394**	**(w) 394**	–	–	–	–	–	–	**(w) 405**	–	**(w) 397**	Ag,Bg	**lattice**
(w) 418	**(w) 421**	**(w) 421**	**(m) 422**	**(w) 413**	**(w) 411**	**(m) 412**	**(w) 416**	**(m) 418**	**(m) 417**	–	**(m) 418**	**(m) 425**	**(w) 420**	**(m) 417**	Ag,Bg	**lattice**
(m) 464	**(w) 472**	**(w) 471**	**(w) 470**	**(m) 462**	**(m) 463**	**(m) 462**	**(m) 466**	**(m) 466**	**(s) 465**	**(m) 464**	–	**(w) 473**	**(w) 466**	**(w) 467**	Ag,Bg	$\nu_2(PO_4)$
(w) 565	**–**	–	–	–	–	**(w) 567**	–	**(w) 571**	–	–	–	**(w) 579**	–	**(w) 572**	–	–
(w) 621	**(w) 626**	**(w) 626**	**(w) 626**	**(w) 617**	**(w) 617**	**(w) 617**	**(w) 621**	**(w) 622**	–	–	–	**(w) 629**	**(w) 623**	**(w) 621**	Ag,Bg	$\nu_4(PO_4)$
sh(w) 961	**sh(w) 972**	**sh(w) 973**	**sh(w) 971**	**sh(w) 962**	**sh(w) 960**	**sh(w) 961**	**sh(w) 963**	**sh(m) 968**	**sh(m) 968**	**sh(m) 970**	**sh(m) 969**	**sh(m) 976**	**sh(m) 971**	**sh(w) 967**	–	–
(s) 973	–	–	–	**(s) 970**	**(s) 969**	**(s) 970**	**(s) 973**	**(s) 974**	**(s) 975**	**(s) 976**	**(s) 975**	**(s) 982**	**(s) 978**	**(s) 975**	Ag,Bg	$\nu_1(PO_4)$
	(s) 978	**(s) 978**	**(s) 979**	–	–	–	–	–	–	–	–	**–**	–	**sh(w) 987**	–	–
sh(w) 994	**(w) 996**	**(w) 997**	**sh(w) 992**	**sh(w) 989**	**(w) 989**	**sh(w) 980**	**sh(w) 991**	–	–	–	–	**–**	–	–	–	–
	–	–	**(w) 1040**	–	**(w) 1054**	**(m) 1055**	–	–	–	–	–	–	–	–	–	–
(w) 1067	**(m) 1063**	**(m) 1063**	**(m) 1066**	**(w) 1065**	–	**(w) 1067**	–	**(m) 1063**	–	–	**(w) 1066**	**(w) 1069**	**(w) 1065**	**(w) 1061**	Ag,Bg	$\nu_3(PO_4)$
	sh(w) 1078	**sh(w) 1080**	**sh(w) 1079**	–	**(w) 1070**	–	–	–	–	–	–	**sh(w) 1084**	–	**sh(w) 1076**	–	–
mid–range luminescence effects																
l(w) 1754	–	–	l,sh(w) 1819	–	–	l,sh(w) 1767	–	–	–	–	–	–	–	–	–	–
l(w) 1911	l(w) 1903	l(w) 1897	l(w) 1917	–	–	l(w) 1910	–	–	–	–	–	l(w) 1917	–	–	–	–
l(w) 2030	l(w) 2036	l(w) 2031	l(w) 2029	l(w) 2024	l(w) 2022	l(w) 2029	l(w) 2034	l(m) 2055	l(m) 2033	l(m) 2052	l(m) 2032	l(w) 2031	–	l(w) 2028	–	–
l(w) 2156	l,sh(w) 2135	l,sh(w) 2116	l,sh(w) 2127	–	–	l,sh(w) 2101	–	–	–	–	l,sh(m) 2097	l,sh(w) 2125	–	–	–	–
–	–	–	–	–	–	f,sh(w) 2307	–	–	–	–	–	–	–	–	–	–

Notes:

[1] – data collected with instrument A corresponding to spectra in Figure 2 and corresponding Raman spots in Figure S3;

[2] – band assignment after data of $LaPO_4$ – $GdPO_4$ end-members (Tab. 3) and according to previous studies (Begun *et al*., 1981; Silva *et al*., 2006).

In bold – Raman bands; l – luminescence bands; sh – shoulders. Intensities of presented data are normalised to $\nu_1(PO_4)$ band equal to 1.0: weak (w) 0.05–0.2, medium (m) 0.2–0.5, strong (s) 0.5–1.0, very strong (vs) >1.0. Only significant signals above background are presented.

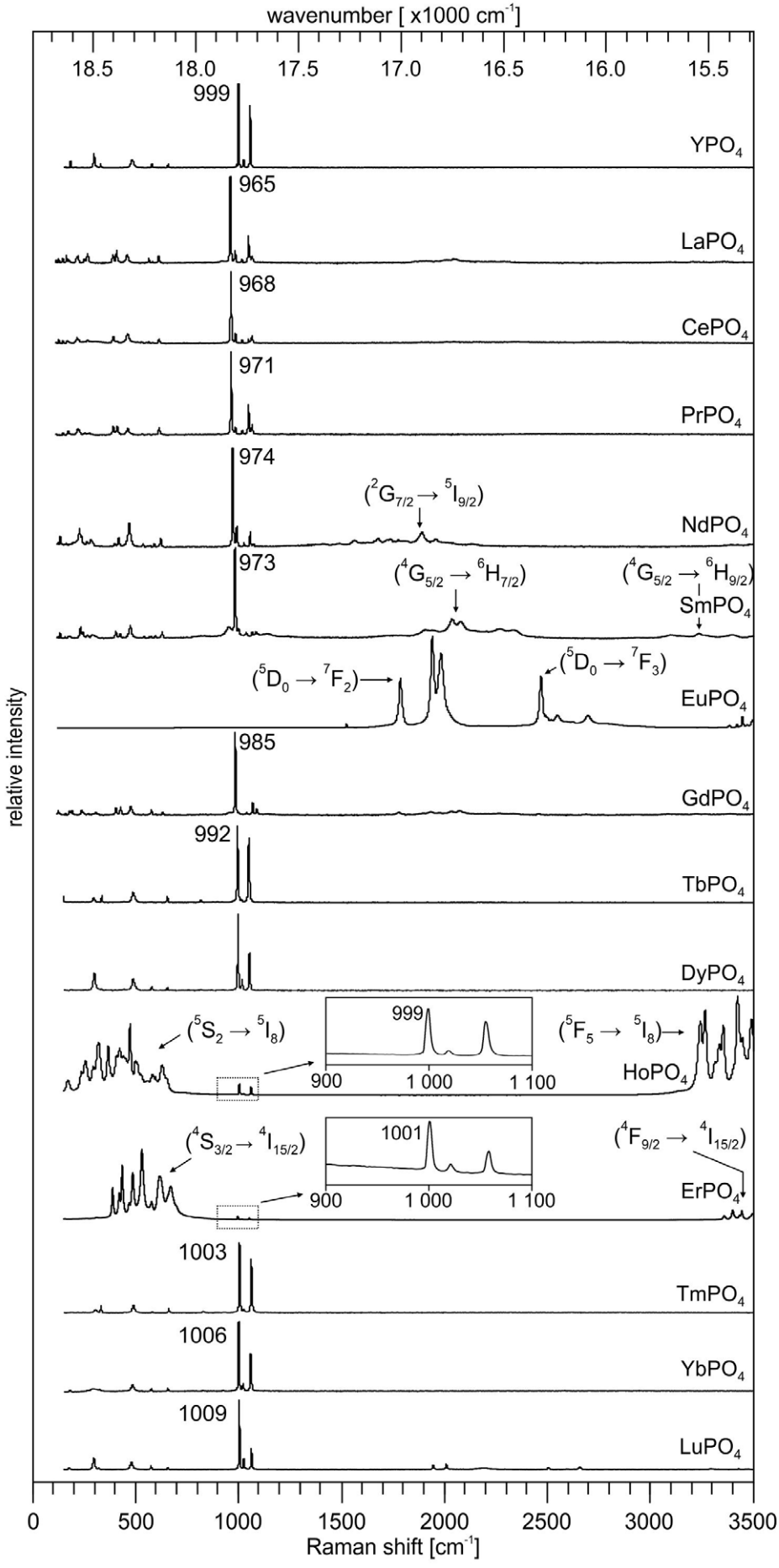

Fig. 1. Raman spectra of synthetic $LaPO_4$–$LuPO_4$ collected with instrument A (532 nm).

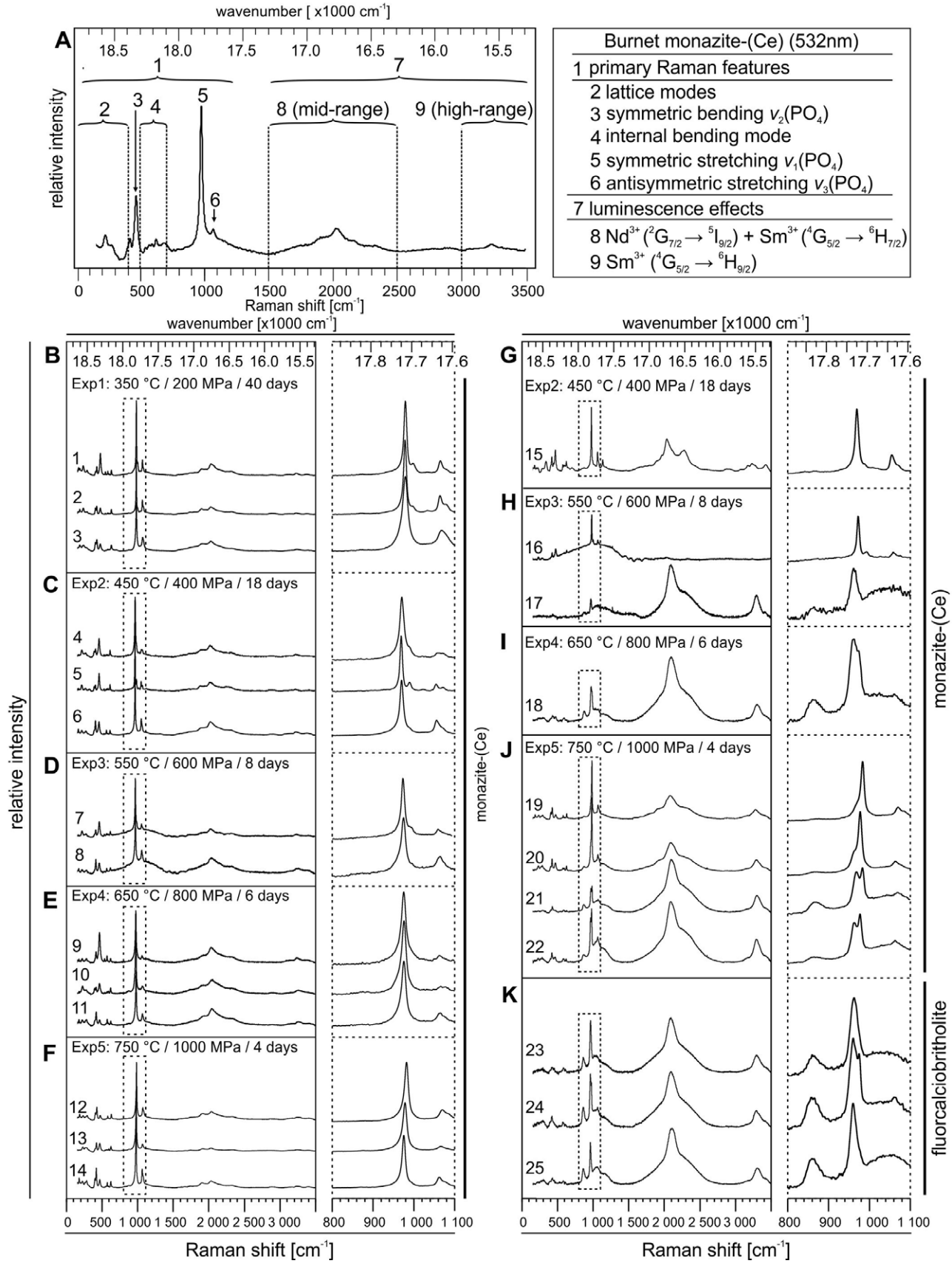

Fig. 2. Raman spectra obtained with instrument A (532 nm) of (**A**) the Burnet monazite-(Ce) and (**B–J**) monazite-(Ce) from experimental products obtained with instrument. **B–F**. Raman spectra of monazite-(Ce), which display similar characteristics as the spectrum of Burnet monazite-(Ce), which can be divided into primary Raman features (150–1200 cm^{-1}) and luminescence effects at mid-range 1500–2500 cm^{-1} and high-range 3000–3500 cm^{-1}, are collected in the core and rim of monazite-(Ce) grains. **G–J**. Raman spectra, which demonstrate major differences compared to the spectrum of the Burnet monazite-(Ce), were collected close to secondary phases. **K**. Fluorcalciobritholite spectra from experimental products of Exp4–Exp5. Right side – zoomed-in spectra corresponding to dotted rectangles.

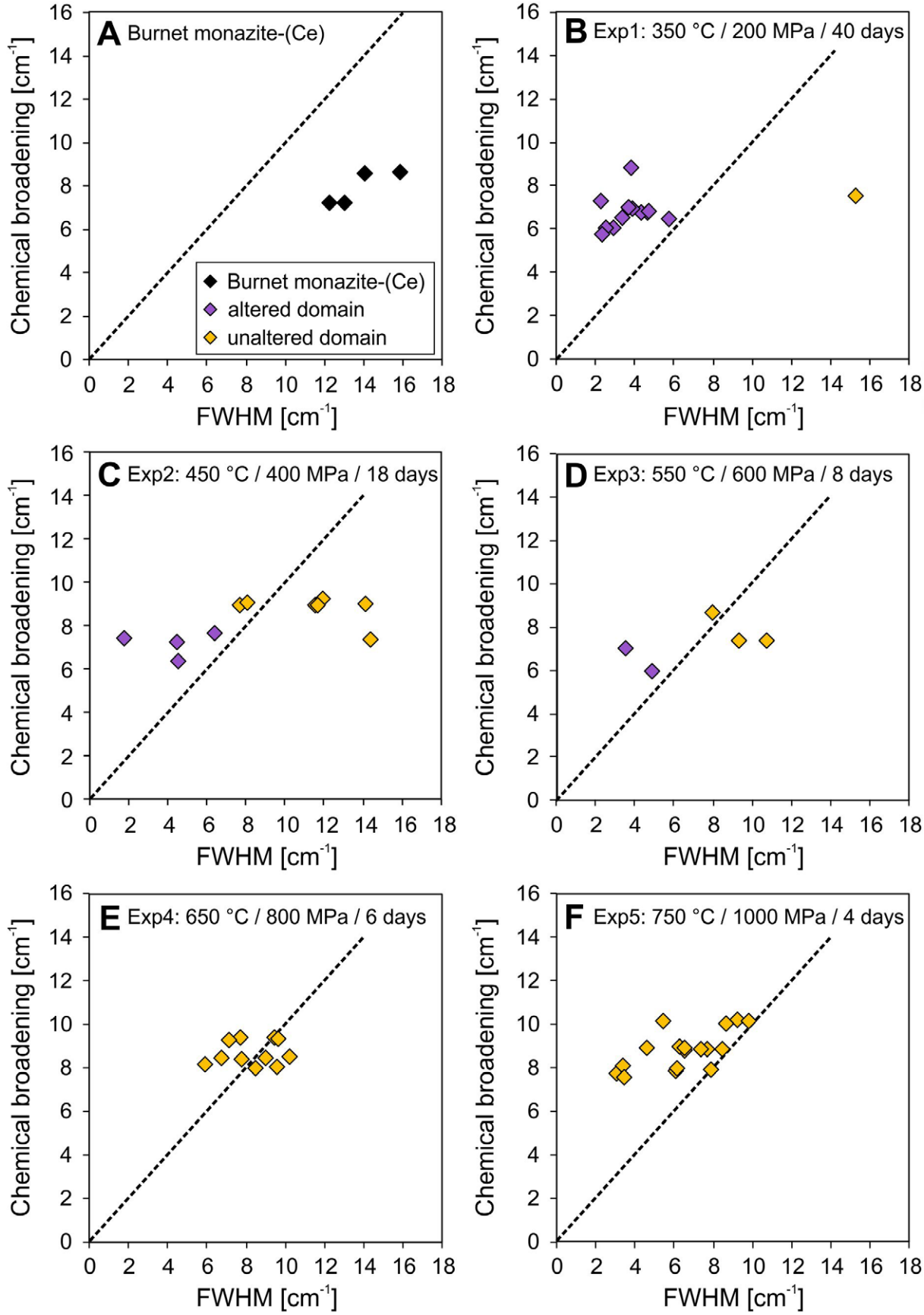

Fig. 3. Measured FWHM values of $\nu_1(PO_4)$ symmetric stretching band vs. chemical broadening of Burnet monazite-(Ce) and monazite-(Ce) from experimental products. The chemical broadening is calculated based on compositional EPMA data using FWHM [cm^{-1}] = 3.95 + 26.66 × (Th + U + Ca + Pb) [apfu] after Ruschel *et al.* (2012).

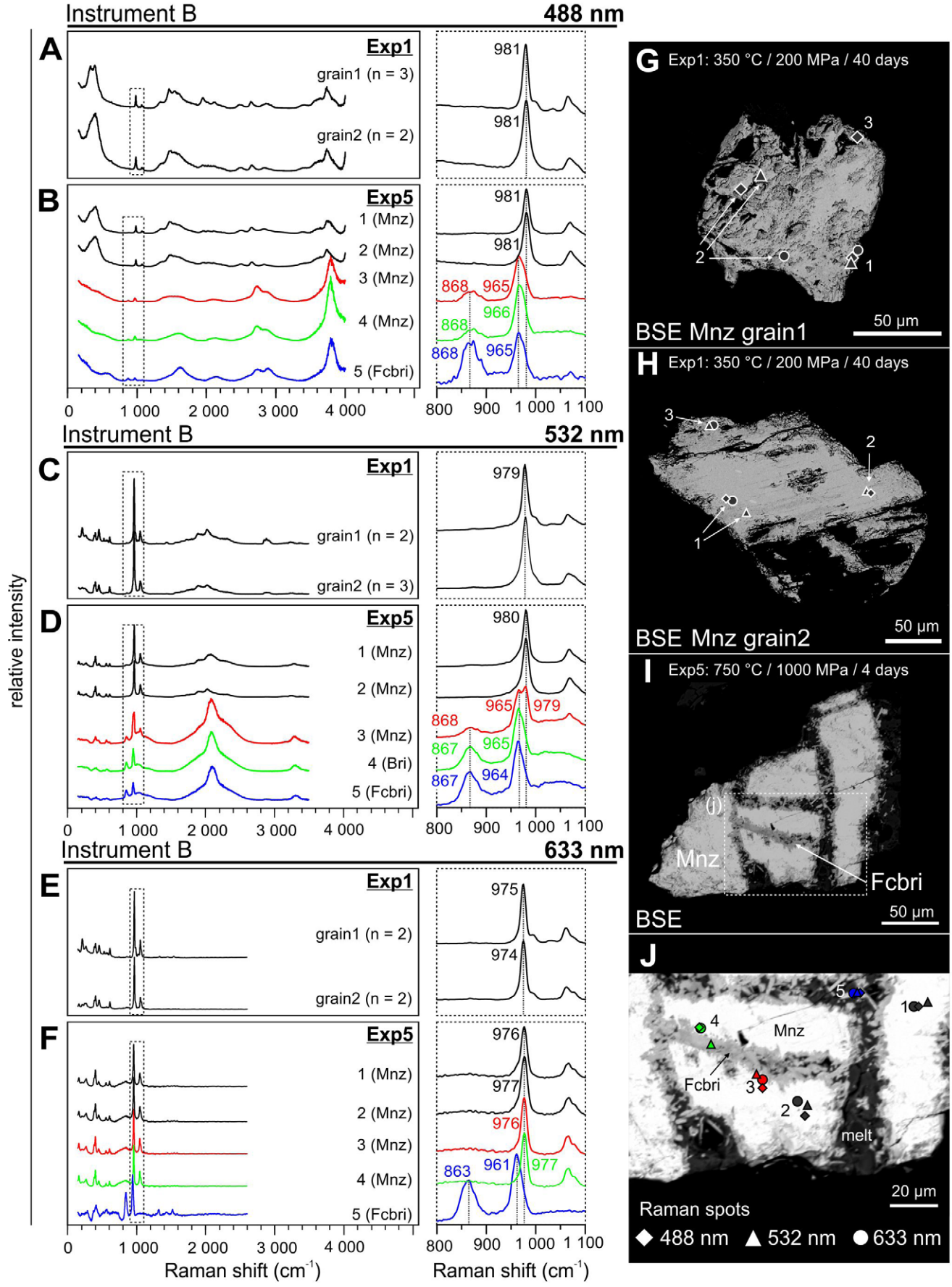

Fig. 4. Raman spectra of selected monazite-(Ce) grains from Exp1 and Exp5 collected with instrument B. **A**, **B**. 488 nm. **C**, **D**. 532 nm. **E**, **F**. 633 nm. Right side – detailed spectra from 900 to 1100 cm^{-1} corresponding to dotted rectangles. **G**–**J**. BSE images of monazite-(Ce) with marked Raman spots. Diamonds – 488 nm laser, triangles – 532 nm laser, circles – 633 nm laser. Mineral abbreviations: Fcbri – fluorcalciobritholite, Mnz – monazite-(Ce).

Raman microspectroscopy of monazite-(Ce) from experimental products was applied to grains in the core and rim, and closely to the reaction front where secondary phases (e.g., steacyite or fluorcalciobritholite) are present. Unaltered and altered domains were distinguished based on compositional and textural evidence for fluid-induced alteration (Supplementary Figs S1, S3). These include dissolution pits, developed microporosity and the formation of secondary phases. For detailed textural and compositional characteristics of monazite-(Ce) and xenotime-(Y) from experimental products, see Supplementary Materials (Supplementary Figs S1–S4; Tabs S3, S4, S6, S7).

Monazite-(Ce) spectra from experimental products resemble the Burnet monazite-(Ce) with only minor variations (Fig. 2B–F). These include small variations of intensities in the range of lattice modes, symmetric bending mode $v_2(PO_4)$ and luminescence effects at mid- and high-range. Band positions of the $v_1(PO_4)$ symmetric stretching band range from 969 to 982 cm^{-1} compared to that of the Burnet monazite-(Ce) at 973 cm^{-1} (Tab. 5). Monazite-(Ce) spectra from Exp3 and Exp4 (600 MPa / 550 °C and 800 MPa / 650 °C) show an overall increased background at 800–1200 cm^{-1} caused by luminescence effects (spectra 7 and 8 in Fig. 2D), and elevated luminescence effects at mid-range (spectra 8–11 in Fig. 2D, E).

Some monazite-(Ce) spectra from Exp2–Exp5, collected closely to secondary phases, show significant differences compared to the Burnet monazite-(Ce) (Fig. 2G–J). A monazite-(Ce) spectrum, collected near secondary REE-rich steacyite (Raman spots 50–52 in Supplementary Fig. S1H), displays an additional distinct band at 1129 cm^{-1} and increased intensity and broadening of mid- and high-range luminescence effects (spectrum 15 in Fig. 2G). The shape of luminescence effects at mid-range differs significantly from those of the Burnet monazite-(Ce) and displays an asymmetric band at 2027 cm^{-1} and a broad band at 2271 cm^{-1} (Fig. 2G).

Some monazite-(Ce) spectra from Exp3–Exp5, collected closely to secondary fluorcalciobritholite, also show significant changes compared to those of the Burnet monazite-(Ce) (Fig. 2H–J). These include (i) increased background at 800–1200 cm^{-1}, (ii) the appearance of a band at ca. 869 cm^{-1} and (iii) a significant increase of intensity and broadening of luminescence effects at mid- and high-range (Fig. 2H–J; Tab. 5). Positions of the $v_1(PO_4)$ symmetric stretching bands range from 969 to 983 cm^{-1} (Tab. 5). However, some spectra display a shift towards lower wavenumbers (962–963 cm^{-1}; spectra 17, 18 in Fig. 2H, I) or a shoulder at that location (spectra 19, 20 in Fig. 2J; Tab. 5). Two spectra show splitting into two bands at ca. 965 cm^{-1} and 975 cm^{-1} (spectra 21, 22 in Fig. 2J).

The shape of mid-range luminescence effects of these spectra resembles that of the Burnet monazite-(Ce) but are of higher intensity, with one dominant band and two asymmetric shoulders (spectra 17, 18, 21, 22 in Fig. 2H–J). The dominant luminescence band, however, is shifted towards a higher Raman shift 2081–2099 cm^{-1} compared to 2028 cm^{-1} in the Burnet monazite-(Ce) and the shoulder at ca. 2260 cm^{-1} is more pronounced. Mid-range luminescence effects of two other spectra possess lesser pronounced luminescence bands and resemble closer those of Burnet monazite-(Ce) (spectra 19, 20 in Fig. 2J). One spectrum, collected in the patchy-zoned monazite-(Ce) (Raman spot 62 in Supplementary Fig. S1L), shows a broad increase in background luminescence at 300–1500 cm^{-1} and disappearance of mid- and high-range luminescence effects (spectrum 16 in Fig. 2H).

The spectral differences observed in some monazite-(Ce) spectra from Exp3–Exp5 are reflected in fluorcalciobritholite spectra (Fig. 2H–K). These display (i) a distinct band at 861–863 cm^{-1}, (ii) luminescence effects which elevate the background at 800–1200 cm^{-1}, (iii) prominent luminescence effects at mid-range with a dominant band at ca. 2100 cm^{-1} and (iv) a distinct luminescence band at high-range. The dominant band of fluorcalciobritholite is positioned at 960–962 cm^{-1}, with one spectrum demonstrating splitting into two bands (960 cm^{-1} and 975 cm^{-1}; Tab. 5; spectra 23–25 in Fig. 2K). Due to the small size of fluorcalciobritholite grains, a mixture of representative fluorcalciobritholite spectra with those of underlying monazite-(Ce) cannot be excluded.

Broadening of the $v_1(PO_4)$ symmetric stretching band of monazite-(Ce) can be caused by distortion of the lattice by incorporation of Th, U, Ca and Pb (Ruschel *et al.,* 2012) The distortion effect (henceforth, chemical broadening) can be calculated with the formula: FWHM [cm^{-1}] = 3.95 + 26.66 × (Th + U + Ca + Pb) [apfu] (Ruschel *et al.,* 2012). Comparison of FWHM values of the $v_1(PO_4)$ band vs. chemical broadening provides valuable information about the structure of monazite-(Ce), particularly the accumulation of radiation damage (Ruschel *et al.,* 2012). The Burnet monazite-(Ce) displays significantly higher FWHM values (12.2–15.9 cm^{-1}) vs. chemical broadening (7.2–8.7 cm^{-1}; Fig. 3A). Monazite-(Ce) from Exp1–Exp3 follows a similar trend in unaltered domains and display FWHM values of 7.9–15.2 cm^{-1} vs. chemical broadening of 7.3–9.2 cm^{-1} (Fig. 3B–D). On the other hand, altered domains demonstrate lower FWHM values (1.7–6.4 cm^{-1}) than chemical broadening (5.8–8.8 cm^{-1}; Fig. 3B–D).

Raman data of monazite-(Ce) from Exp4 and Exp5 belong solely to compositionally unaltered domains and show a wide spread of FWHM values (3.0–12.8 cm^{-1}), which are generally lower than chemical broadening (7.6–10.2 cm^{-1}; Fig. 3E, F). The Raman data of compositionally unaltered domains of all selected experiments (Exp1–Exp5) demonstrate a general trend of decreasing FWHM values with increasing temperature conditions.

A monazite-(Ce) spectrum, collected with the 780 nm laser (instrument A) from Exp1, displays extensive luminescence effects, which completely superimpose the primary Raman features. Thus, the 780 nm laser is considered unsuited for Raman spectroscopic investigations of monazite-(Ce) in this work (for more details see Supplementary Fig. S5).

Comparison of monazite-(Ce) spectra from Exp1 and Exp5 – instrument B (488 nm, 532 nm and 633 nm lasers)

Two grains of monazite-(Ce) from Exp1 and a cluster of monazite-(Ce) grains from Exp5, which are embedded in residual glass, were selected for analyses with instrument B using 488 nm, 532 nm and 633 nm lasers (Fig. 4). Monazite-(Ce)

spectra (488 nm) show significant luminescence effects, which superimpose the primary Raman features (Fig. 4A, B). The $\nu_1(PO_4)$ band of grains of Exp1 and in the core of monazite-(Ce) from Exp5 is located at 981 cm^{-1} (grains 1 and 2, spectra 1 and 2 in Fig. 4A, B). The $\nu_1(PO_4)$ bands of monazite-(Ce) spectra, collected closely to fluorcalciobritholite, are shifted to 965–966 cm^{-1} together with a new band at 868 cm^{-1}, which correspond to the dominant bands of the fluorcalciobritholite spectrum at 965 cm^{-1} and 868 cm^{-1} (spectra 3–5 in Fig. 4B).

The monazite-(Ce) spectra collected with instrument B (532 nm) generally show the same features as spectra measured with instrument A (Fig. 4C, D). However, the spectra from Exp1 show additional luminescence effects at 2900–3000 cm^{-1}, which are not documented in any Raman spectrum from instrument A. A monazite-(Ce) spectrum close to fluorcalciobritholite shows the splitting of the $\nu_1(PO_4)$ band into two bands (965 cm^{-1} and 979 cm^{-1}) and a weak band at 868 cm^{-1} (spectrum 3; Fig. 4D).

Spectra collected with the 633 nm laser, display the least luminescence effects from 1100–2600 cm^{-1} compared to other excitation lasers (Fig. 4E, F). Spectra of monazite-(Ce) from Exp5, display an increased background in the range of 750–1000 cm^{-1} (Fig. 4F). All band positions are slightly shifted towards lower wavenumbers, compared to spectra collected with 488 nm and 532 nm lasers, with the $\nu_1(PO_4)$ band located at 974–976 cm^{-1} and the dominant bands of fluorcalciobritholite at 863 cm^{-1} and 961 cm^{-1}.

Compositional and Raman characteristics of the Ankazobe monazite-(Ce) – instrument A (532 nm laser)

The Ankazobe monazite-(Ce) contains unaltered domains, mostly homogeneous in BSE imaging, and altered porous domains (Fig. 5A–C). Numerous inclusions of xenotime-(Y), mica with a composition similar to phengite, and Th-silicate accompany the extensively altered domain. The unaltered domains of Ankazobe monazite-(Ce) display a composition typical for common monazite-(Ce) (25.83–26.41 wt.% Ce_2O_3, 7.19–7.58 wt.% ThO_2, 0.33–0.38 wt.% UO_2 and 0.17–0.19 wt.% PbO; Supplementary Tab. S3). Altered domains contain 26.33–32.81 wt.% Ce_2O_3 and are depleted in Th, U and Pb (5.00–7.18 wt.% ThO_2, 0.07–0.17 wt.% UO_2 and 0.11–0.16 wt.% PbO; Supplementary Tab. S3).

Raman spectra of unaltered domains of the Ankazobe monazite-(Ce) are similar to that of the Burnet monazite-(Ce). Similarities include (i) lattice modes, (ii) pronounced internal bending modes (500–700 cm^{-1}), (iii) a lesser symmetric bending $\nu_2(PO_4)$ mode at 466 cm^{-1}, (iv) the $\nu_1(PO_4)$ band at 976 cm^{-1} and (v) similar luminescence effects at mid-range, but no luminescence effects present at high-range (Fig. 5D). Spectra of altered domains show increased background-luminescence (800–1500 cm^{-1}) and either a low-intensity spectrum with negligible mid-range luminescence effects or a spectrum with a new broad band at ca. 1325 cm^{-1} (spectrum 27 in Fig. 5D). Unaltered domains of the Ankazobe monazite-(Ce) show generally higher FWHM values (10.5–13.2 cm^{-1}) than chemical broadening (6.5–6.6 cm^{-1}), whereas altered domains follow this trend to a lesser degree (6.3–10.2 cm^{-1} FWHM vs. 4.3–6.3 cm^{-1} chemical broadening; Fig. 5E).

Hyperspectral maps of monazite-(Ce) – instrument B (532 nm and 633 nm lasers)

Hyperspectral maps (instrument B; 1 µm step size) were collected with 532 nm and 633 nm lasers in selected areas of monazite-(Ce) grains from Exp5 (1000 MPa / 750 °C; Fig. 6). The monazite-(Ce) grains are embedded in residual glass from partial melting. Secondary fluorcalciobritholite formed in the gaps between monazite-(Ce) grains, dissolution pits and micropores at the monazite-(Ce) rim (Fig. 6; Supplementary Fig. S1W, X). True compound analysis (TCA) images were achieved by combining characteristic spectra of various phases. The TCA image correlates well with the BSE image (Fig. 6A–C). Intensity maps (532 nm and 633 nm) of the $\nu_1(PO_4)$ band reveal two domains in monazite-(Ce), one at 978 cm^{-1} and a domain with a significant shift towards lower wavenumbers 962 cm^{-1} (Fig. 6F–J). The EPMA-WDS compositional X-ray maps, collected at the same location as the hyperspectral maps, demonstrate only small compositional variations (Fig. 7). The monazite-(Ce) is homogeneous and contains Th-rich microinclusions in the rim (Fig. 7B).

Raman microspectroscopy of NWFP xenotime-(Y) and xenotime-(Y) from experimental products (Exp1–Exp5) – instrument A (532 nm laser)

The NWFP xenotime-(Y) spectrum is composed of (i) primary Raman features including the $\nu_1(PO_4)$ symmetric stretching band and the $\nu_3(PO_4)$ antisymmetric stretching band, and (ii) strong luminescence effects, which superimpose the lattice modes and internal bending modes at low-range (100–800 cm^{-1}; Fig. 8A; Tab. 6). The NWFP xenotime-(Y) shows weak to moderate luminescence signals at mid-range (1500–3000 cm^{-1}), which are contributed by Eu^{3+}, Sm^{3+} electronic transitions (Figs 1, 8A; cf. Lenz *et al*., 2015), whereas moderate to strong luminescence effects at high-range (3000–3500 cm^{-1}) are contributed by Sm^{3+} and Ho^{3+} ions (Figs 1, 8A; cf. Lenz *et al.,* 2015).

Raman microspectroscopy of xenotime-(Y) from experimental products was applied to xenotime-(Y) grains as described for monazite-(Ce) above. Most xenotime-(Y) spectra from experimental products are very similar to the spectrum of NWFP xenotime-(Y) (spectra 1–4, 7 in Fig. 8B–F; Tab. 7). However, some xenotime-(Y) spectra from experiments Exp4 and Exp5 (800 MPa / 650 °C, 1000 MPa / 750 °C) show significant differences (spectra 5, 6, 8, 9 in Fig. 8E, F; Tab. 7). These include broadening of Ho^{3+} and Er^{3+} luminescence bands at low-range and luminescence effects of Eu^{3+} at mid-range. Furthermore, the Eu^{3+} ($^5D_0 \rightarrow {}^7F_3$) luminescence band displays significant broadening and increase of intensity at ca. 2650 cm^{-1} in two spectra (spectra 6 and 9 in Fig. 8E, F). These spectra also show the appearance of a broad shoulder at ca. 800 cm^{-1}. The $\nu_1(PO_4)$ band of xenotime-(Y) is located at a narrow range of 1000–1001 cm^{-1}. Occasionally, a subtle band is present at ca. 967 cm^{-1}

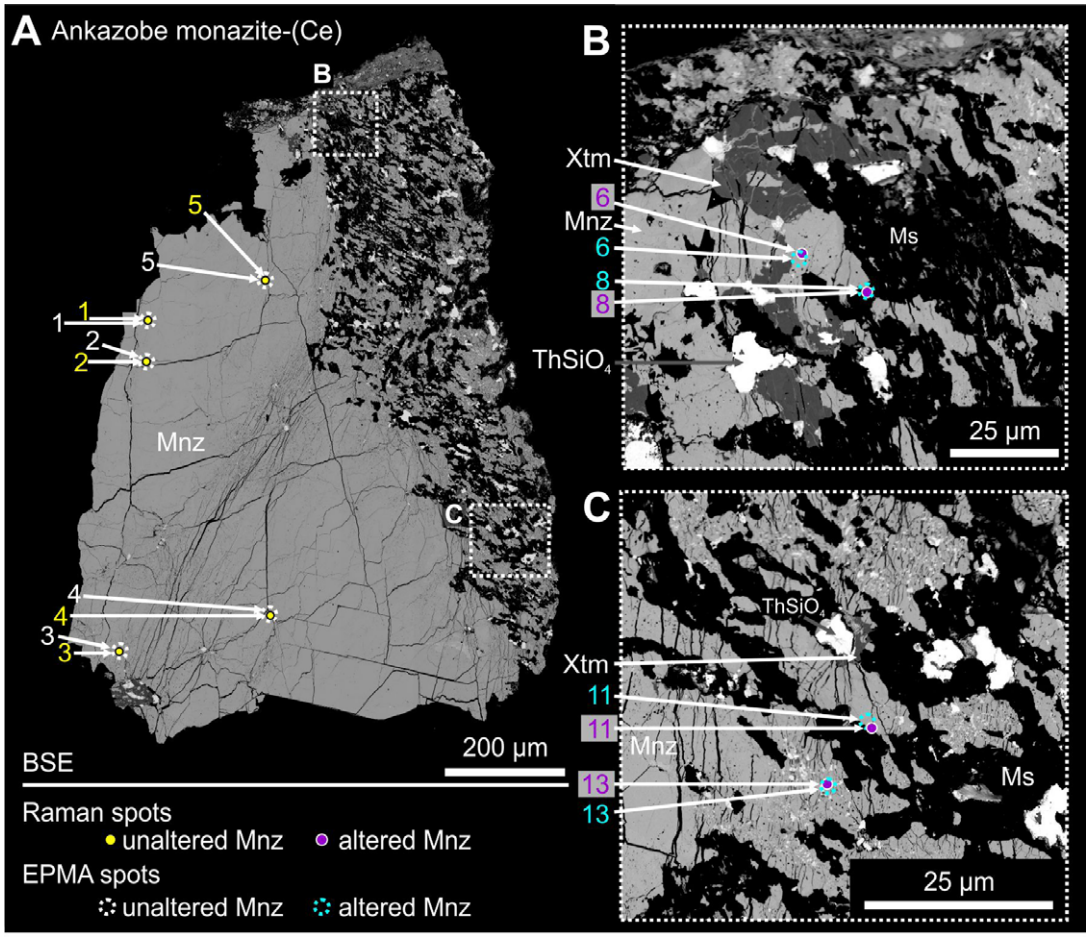

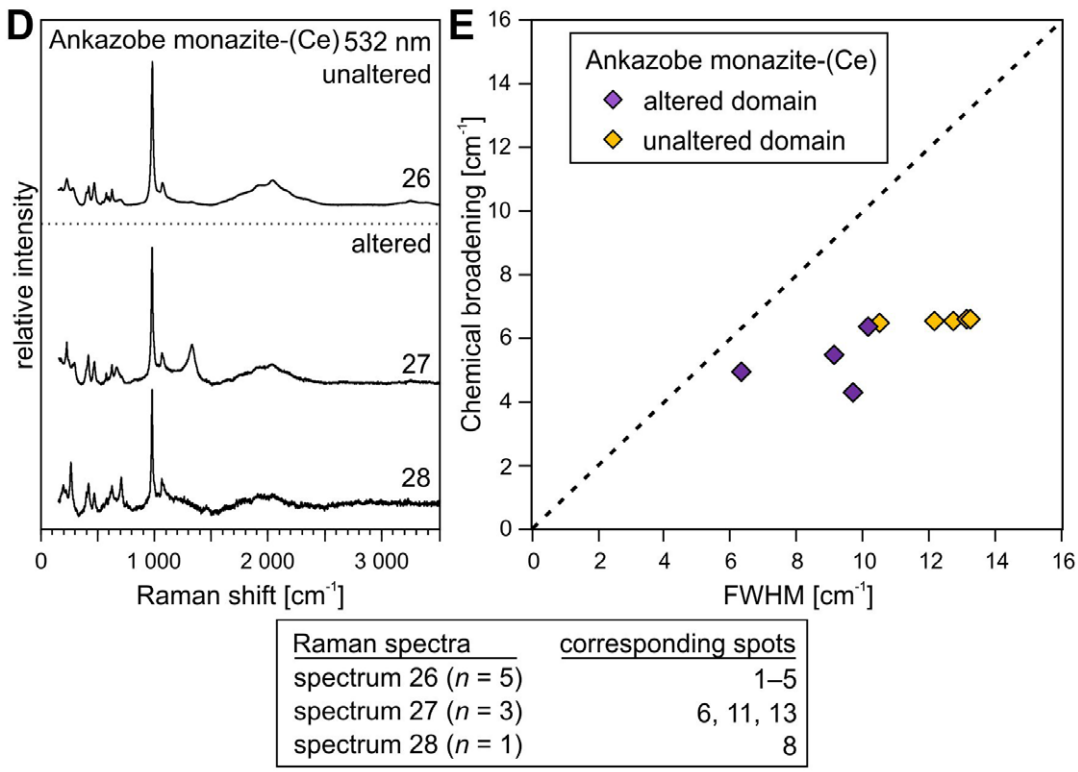

Raman spectra	corresponding spots
spectrum 26 (*n* = 5)	1–5
spectrum 27 (*n* = 3)	6, 11, 13
spectrum 28 (*n* = 1)	8

Fig. 5. BSE images and Raman data of monazite-(Ce) from Ankazobe (Madagascar). **A**. Homogeneous unaltered domains. **B**, **C**. Altered domains of monazite-(Ce) containing inclusions of xenotime-(Y), mica with a composition similar to phengite, and Th-silicate. **D**. Raman spectra of unaltered domains similar to those of the Burnet monazite-(Ce) (Fig. 1), whereas spectral variations are present in altered domains. **E**. FWHM values vs. chemical broadening calculated with compositional EPMA data using FWHM [cm^{-1}] = 3.95 + 26.66 × (Th + U + Ca + Pb) [apfu] after Ruschel *et al.* (2012). Mineral abbreviations: Ms – muscovite (phengite), Mnz – monazite-(Ce) and Xtm – xenotime-(Y).

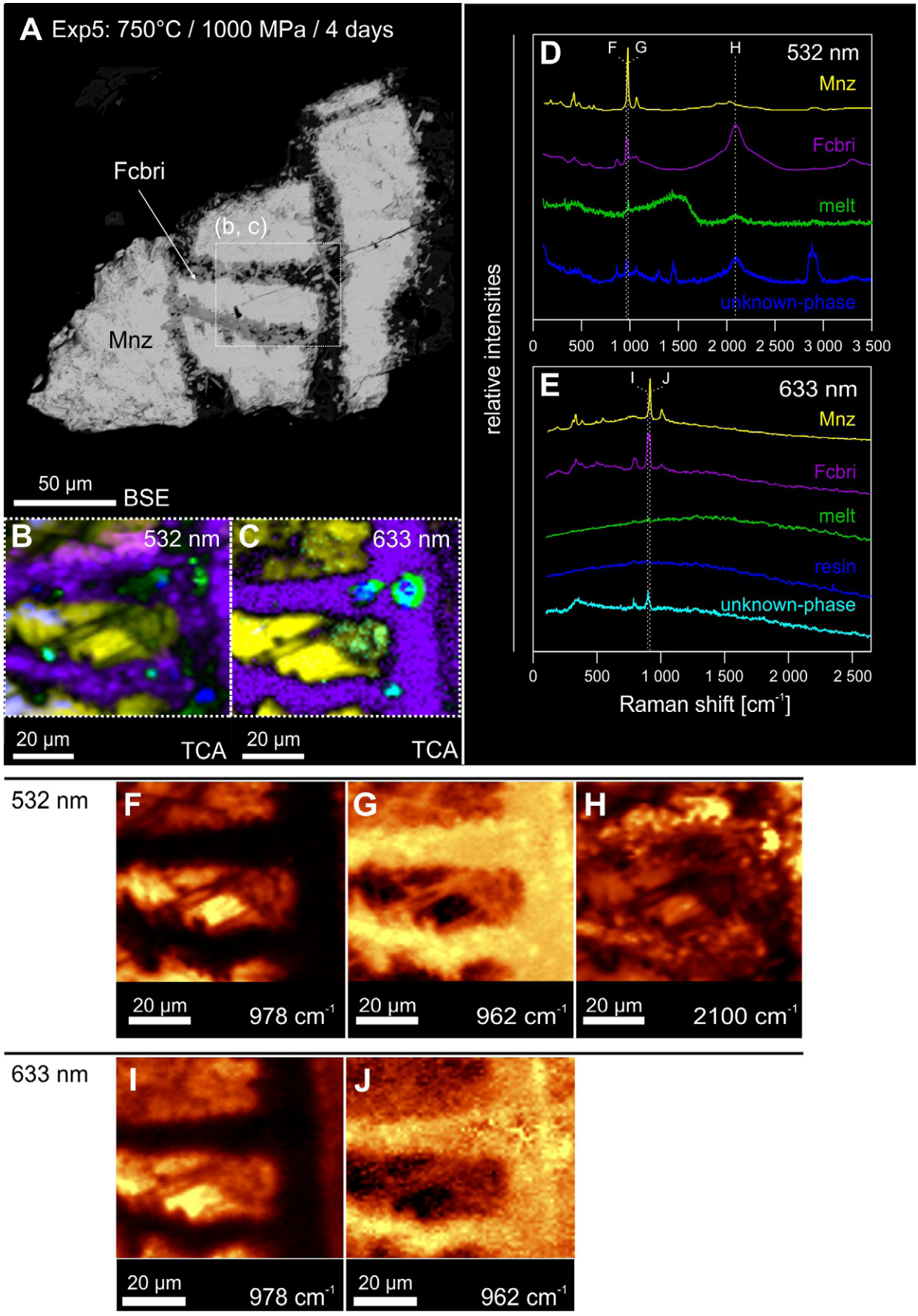

Fig. 6. Hyperspectral maps (instrument B) of monazite-(Ce) from Exp5 (1000 MPa / 750 °C). **A**. BSE image of overview and selected area. **B**, **C**. TCA image of spectral data collected with 532 nm and 633 nm lasers. **D**, **E**. Corresponding Raman spectra of individual phases. **F**–**H**. Intensity maps of selected distinct bands (532 nm). **I**, **J**. Intensity maps of selected bands (633 nm). Abbreviations: Fcbri – fluorcalciobritholite, Mnz – monazite-(Ce).

Table 6

Raman data of monazite-(Ce) (Mnz) and fluorcalciobritholite (Fcbri) from experiments obtained with 532 nm and 633 nm lasers.

Raman spectra and corresponding Raman spots of monazite and fluorcalciobritholite													**Assigned band[1]**	
Exp2 (Mnz)[2]	Exp3 (Mnz)[2]		Exp4 (Mnz)[2]	Exp5 (Mnz)[2]				Exp4–Exp5 (Fcbri)[2]			Exp5 (Mnz)[3]	Exp5 (Fcbri)[3]		
spectrum 15 (n = 3)	spectrum 16 (n = 1)	spectrum 17 (n = 1)	spectrum 18 (n = 3)	spectrum 19 (n = 4)	spectrum 20 (n = 6)	spectrum 21 (n = 2)	spectrum 22 (n = 2)	spectrum 23 (n = 1)	spectrum 24 (n = 1)	spectrum 25 (n = 1)	spectrum 1 (n = 1)	spectrum 5 (n = 1)	symmetry	modes
spot: 50–52	spot: 62	spot: 56	spot: 69, 70, 82	spot: 94, 98, 99, 119	spot: 110–112, 115, 127, 134	spot: 101, 121	spot: 109, 133	spot: 131	spot: 130	spot: 114	spot: 1	spot: 5		
(w) 171	–	–	–	–	–	–	–	–	–	–	**(w) 179**	–	Bg	**lattice**
–	**(w) 224**	–	–	–	**(w) 227**	–	–	–	–	–	–	–	Ag,Bg	**lattice**
–	–	–	–	–	**(w) 282**	–	–	–	**(w) 297**	–	**(w) 286**	–	Ag	**lattice**
(w) 331	–	–	–	–	–	–	–	–	–	–	–	–	–	–
–	–	–	–	–	**(w) 398**	–	–	–	–	–	**(m) 400**	–	Ag,Bg	**lattice**
(m) 412	**(w) 416**	–	–	**(w) 405**	**(w) 419**	–	–	–	–	–	–	–	Ag,Bg	**lattice**
–	–	–	–	**(m) 425**	–	**(m) 425**	**(m) 420**	–	**(m) 419**	–	**(m) 420**	**(m) 424**	Ag,Bg	**lattice**
(m) 461	**(m) 466**	–	–	**(w) 473**	**(w) 466**	–	**(w) 459**	–	–	–	**(w) 467**	–	Ab,Bg	$\nu_2(PO_4)$
(w) 567	–	–	–	–	–	–	–	–	–	–	**(w) 574**	–	–	–
(w) 617	–	–	–	**(w) 628**	**(w) 622**	–	–	–	–	–	**(w) 624**	–	Ag,Bg	$\nu_4(PO_4)$
–	–	–	–	–	–	**(m) 869**	**(w) 868**	**(m) 863**	**(m) 861**	**(m) 862**	–	**(s) 868**	–	–
–	–	**(s) 962**	**(s) 963**	–	**sh(m) 963**	**–**	**(s) 962**	**(s) 962**	**(s) 960**	**(s) 960**	**sh(m) 961**	**(s) 962**	–	–
sh(w) 957	–	–	–	**sh(m) 976**	**–**	**–**	–	–	**(s) 975**	–	**(s) 976**	–	Ag,Bg	$\nu_1(PO_4)$
(s) 969	**(s) 973**	–	–	**(s) 983**	**(s) 977**	**(s) 967**	**(s) 977**	–	–	–	–	–	–	–
sh(w) 984	**sh(w) 993**	–	l(m) 1024	**–**	**sh(w) 990**	**(s) 982**	–	l(m) 1025	l(m) 1014	–	–	–	–	–
(m) 1054	**(w) 1059**	–	–	–	–	l(s) 1040	**(m) 1032**	–	–	l(s) 1046	–	–	–	–
sh(w) 1067	–	–	–	–	**(w) 1063**	–	**(w) 1065**	–	**(w) 1062**	–	**(m) 1064**	–	Ag,Bg	$\nu_3(PO_4)$
–	–	**(vs) 1086**	–	**(w) 1070**	**sh(w) 1078**	–	**(m) 1159**	–	–	–	**(w) 1079**	–	–	–
(w) 1129	–	–	l(s) 1182	–	–	–	–	–	–	l,sh(w) 1181	–	–	–	–
mid–range luminescence effects														
l,sh(w) 1896	–	–	–	l,sh(w) 1809	l,sh(w) 1811	–	l,sh(m) 1833	–	–	–	–	–	–	–
l(m) 2027	–	–	l,sh(s) 1927	l(w) 1919	l,sh(w) 1927	l,sh(s) 1949	l,sh(w) 1935	l,sh(m) 1895	l,sh(m) 1936	l,sh(m) 1962	–	–	–	–
lsh(m) 2085	–	l(vs) 2087	l(vs) 2085	l,sh(m) 2081	l(m) 2084	l(vs) 2099	l(vs) 2088	l(s) 2089	l(s) 2092	l(s) 2101	–	–	–	–
l(m) 2271	–	l,sh(vs) 2261	l,sh(vs) 2230	l,sh(m) 2291	l,sh(m) 2260	l,sh(vs) 2247	l,sh(s) 2245	l,sh(s) 2212	l,sh(s) 2234	l,sh(s) 2253	–	–	–	–
high–range luminescence effects														
–	–	–	–	–	–	–	l,sh(w) 3167	–	–	–	–	–	–	–
l(w) 3235	–	l(vs) 3291	l(s) 3292	l(m) 3289	l(w) 3293	l(s) 3299	l(s) 3293	l(m) 3294	l(m) 3285	l,sh(w) 3202	–	–	–	–
l(w) 3419	–	–	–	–	–	–	l,sh(w) 3404	–	l,sh(w) 3376	l(m) 3309	–	–	–	–
–	–	–	–	–	–	–	–	–	–	l,sh(w) 3423	–	–	–	–

Notes:

[1] – band assignment to monazite after data of $LaPO_4$–$GdPO_4$ end-members (Tab. 3) and according to previous studies (Begun *et al*., 1981; Silva et al., 2006);

[2] – data collected with instrument A (532 nm) corresponding to spectra in Figure 1 and Raman spots in Figure S1;

[3] – data collected with instrument B (633 nm) corresponding to spectra 1 (Mnz) and 5 (Fcbri) in Figure 4F and Raman spots in Figure 4J.

In bold – Raman bands; l – luminescence bands; sh – shoulders, Intensities of presented data are normalised to most dominant Raman band equal to 1.0: weak (w) 0.05–0.2, medium (m) 0.2–0.5, strong (s) 0.5–1.0, very strong (vs) >1.0; sh – shoulders; * – fluorescence. Only significant signals above background are presented.

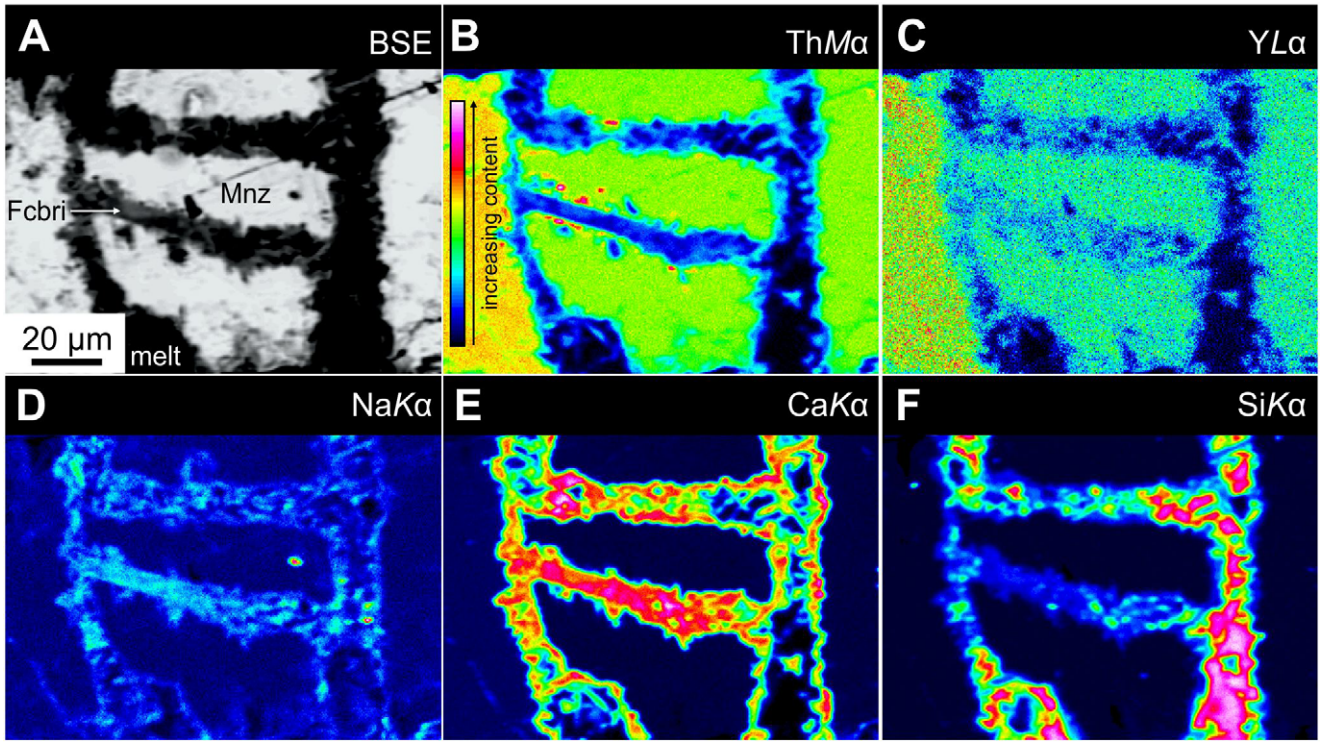

Fig. 7. BSE image and EPMA-WDS compositional X-ray maps of a selected area of monazite-(Ce) from Exp5 (1000 MPa / 750 °C), which correspond to the position of hyperspectral maps. Mineral abbreviations: Fcbri – fluorcalciobritholite, Mnz – monazite-(Ce).

(spectra 5, 6, 8, 9 in Fig. 8E, F; Tab. 7). Raman spectra of Y-rich fluorcalciobritholite generally show higher intensity and broadening of luminescence effects in comparison with xenotime-(Y) spectra, with the most dominant luminescence band potentially caused by Eu^{3+} ($^5D_0 \rightarrow {}^7F_3$) at ca. 2641–2647 cm^{-1} (Fig. 8G).

Weak bands at 966–970 cm^{-1} are interpreted as the primary Raman band of the Y-rich fluorcalciobritholite and are located at a higher Raman shift than Raman bands of fluorcalciobritholite from monazite-(Ce) experiments (960–962 cm^{-1}; Figs 2K, 8G). However, the additional band at ca. 860 cm^{-1}, which was observed in fluorcalciobritholite spectra from monazite-(Ce) experiments, is not present in Y-rich fluorcalciobritholite.

A xenotime-(Y) spectrum (Exp1) collected with the 780 nm laser is dominated by broad low-range luminescence effects caused by Tm^{3+} ($^3H_4 \rightarrow {}^3H_6$) electronic transitions (Supplementary Fig. S6). Due to the extensive luminescence effects present at low-range, the 780 nm laser was not further applied in this work.

Comparison of xenotime-(Y) spectra from Exp1 and Exp5 – instrument B (488 nm, 532 nm, and 633 nm lasers)

Xenotime-(Y) grains from Exp1 and Exp5 were selected for analyses with instrument B using 488 nm, 532 nm and 633 nm lasers. Dominant luminescence effects superimpose xenotime-(Y) spectra using 488 nm. Only the $\nu_1(PO_4)$ symmetric stretching band (B1 – 1006–1007 cm^{-1}) and the $\nu_3(PO_4)$ antisymmetric stretching bands (B2 – 1031 cm^{-1} and B3 – 1064 cm^{-1}) are distinguishable, but show a significant shift towards higher Raman shift compared to band positions of NFWP xenotime-(Y) (B1 – 999 cm^{-1}; B2 – 1023 cm^{-1}; B3 – 1056 cm^{-1}) taken with 532 nm laser (Fig. 9A, B; Tab. 7). The luminescence effects are composed of (i) weak signals at low-range (ca. 100–300 cm^{-1}), (ii) moderate luminescence effects at mid-range (1200–1750 cm^{-1}) followed by a group of 9–10 dominant bands (1800–2500 cm^{-1}), and (iii) weak signals at high-range (3000–4000 cm^{-1}) with one moderate band at ca. 3500 cm^{-1}. In the Y-rich fluorcalciobritholite spectrum, a distinct dominant Raman band is present at 974 cm^{-1} (spectrum 4; Fig. 9B).

Xenotime-(Y) spectra (532 nm) collected with instrument B are similar to those collected with instrument A (Figs 8, 9C, D). Spectra of Y-rich fluorcalciobritholite collected with instrument B show extensively broader luminescence bands at low-range (combined Ho^{3+}: $^5S_2 \rightarrow {}^5I_8$ and Er^{3+}: $^4S_{3/2} \rightarrow {}^4I_{15/2}$) compared to spectra collected with instrument A, which completely superimpose all Raman signals (Figs 8G, 9D). Luminescence effects at mid-range, however, are less pronounced in spectra collected with instrument B.

Xenotime-(Y) spectra (633 nm) show strong luminescence effects at low-range (100–900 cm^{-1}) and weak luminescence effects at mid-range (ca. 1300–1700 cm^{-1}; Fig. 9E, F). The $\nu_1(PO_4)$ symmetric stretching band is located at 1001–1002 cm^{-1} and antisymmetric stretching bands at ca. 1026 cm^{-1} and ca. 1060 cm^{-1} (Fig. 9E, F). The low-range luminescence effects are caused by contributions of electronic transitions of Ho^{3+} ($^5F_5 \rightarrow {}^5I_8$) and Er^{3+} ($^4F_{9/2} \rightarrow {}^4I_{15/2}$) (Lenz *et al.,* 2015). Spectra of Y-rich fluorcalciobritholite reveal broad luminescence effects at low-range (ca. 100–900 cm^{-1}) and distinct primary bands at 968–969 cm^{-1} (Fig. 9F).

Table 7

Raman data of NWFP xenotime-(Y), xenotime-(Y) from experiments and Y-rich fluorcalciobritholite from experiments (532 nm laser).

Raman spectra and corresponding Raman spots of xenotime-(Y) and Y-rich fluorcalciobritholite[1)]												
NWFP xenotime–(Y)	Xenotime-(Y)									Y-rich fluorcalciobritholite		
	Exp1	Exp2	Exp3	Exp4			Exp5			Exp4, Exp5		
(n = 3)	spec. 1 (n = 17)	spec. 2 (n = 10)	spec. 3 (n = 21)	spec. 4 (n = 4)	spec. 5 (n = 1)	spec. 6 (n = 3)	spec. 7 (n = 9)	spec. 8 (n = 2)	spec. 9 (n = 2)	spec. 10 (n = 2)	spec. 11 (n = 2)	spec. 12 (n = 4)
	spots: 1–18	spots: 19–28	spots: 29–46, 48–50	spots: 51–53, 58	spot: 59	spots: 54, 55, 59	spots: 61, 62, 64, 67, 68, 71, 78–80	spots: 70, 75	spots: 63, 72	spots: 56, 60	spots: 74, 77	spots: 65, 66, 69, 73
l(m) 231	l(m) 233	l(m) 233	l(w) 233	l(m) 234	l(m) 235	l(m) 235	l(m) 234	l(m) 234	–	–	–	–
l(m) 250	l(s) 250	l(m) 251	l(m) 252	l(m) 251	l(s) 252	l(m) 252	l(m) 251	l(s) 251	l(m) 252	–	–	–
l(w) 295	l(s) 298	l(m) 298	l(m) 297	l(m) 298	–	–	l(s) 298	l(s) 299	–	–	–	–
l(m) 314	l(s) 315	l(m) 315	l(m) 316	l(m) 316	l(vs) 317	l(s) 317	l(s) 315	l(s) 315	l(s) 317	–	–	–
l(vs) 373	–	l(m) 330	l(m) 331	l(m) 330	–	l(s) 331	l(m) 330	–	l(s) 331	–	l(s) 340	l(m) 334
l(s) 406	l(vs) 375	l(vs) 375	l(vs) 375	l(vs) 375	l(vs) 376	l(vs) 376	l(vs) 375	l(vs) 375	l(vs) 375	l(s) 352	–	–
–	l(vs) 407	l(vs) 407	l(s) 407	l(vs) 408	l(vs) 408	l(vs) 408	l(vs) 408	l(vs) 408	l(vs) 408	l(w) 376	–	l,sh(m) 376
l(vs) 425	l(vs) 426	l(vs) 426	l(vs) 426	l(vs) 426	l(vs) 426	l(vs) 426	l(vs) 426	l(vs) 426	l(vs) 426	l(m) 428	–	l(m) 421
l(m) 456	l(vs) 458	l(s) 458	l(vs) 458	l(vs) 458	l(vs) 458	l(vs) 458	l(vs) 458	l(vs) 458	l(vs) 459	–	l,sh(vs)443	l,sh(m) 466
l(vs) 477	l(vs) 478	l(vs) 478	l(vs) 477	l(vs) 478	l(vs) 478	l(vs) 478	l(vs) 478	l(vs) 478	l(vs) 478	–	l(s) 506	l(m) 501
l(vs) 519	l(vs) 520	l(vs) 520	l(vs) 520	l(vs) 520	l(vs) 520	l(vs) 520	l(vs) 520	l(vs) 520	l(vs) 520	l(vs) 503	l(s) 550	l(m) 546
l(m) 570	l(vs) 572	l(s) 572	l(vs) 571	l(vs) 572	l(vs) 571	l(vs) 572	l(vs) 572	l(vs) 572	l(vs) 572	–	l(s) 595	l,sh(m) 595
l(vs) 609	l(vs) 607	l(vs) 608	l(vs) 609	l(vs) 609	l(vs) 608	l(vs) 610	l(vs) 608	l(vs) 608	l(vs) 609	l(s) 600	l(vs) 666	l(s) 668
–	l(vs) 666	l(vs) 666	l(vs) 665	l(vs) 665	l(vs) 666	l(vs) 666	l(vs) 666	l(vs) 666	l(vs) 666	l(vs) 670	–	–
–	–	–	–	–	–	–	–	–	–	l(vs) 769	I,sh(vs)769	l(s) 772
–	–	–	–	–	–	–	–	–	–	l(m) 875	l(m) 878	lsh(m) 874
–	–	–	–	–	**(w)967**	–	–	–	**(w) 966**	**(w) 970**	**(w) 966**	**(w) 967**
(s) 999	**(s) 1000**	**(s) 1000**	**(s) 1000**	**(s) 1000**	**(s) 1001**	**(s) 1001**	**(s) 1000**	**(s) 1000**	**(s) 1001**	**(w) 1000**	–	–
(w) 1023	**(w) 1025**	**(w) 1025**	**(w) 1024**	**(w) 1025**	**(w) 1025**	**(w) 1025**	**(w) 1025**	**(w) 1025**	**(w) 1025**	–	–	–
(s) 1056	**(m) 1058**	**(s) 1058**	**(s) 1058**	**(s) 1058**	**(m) 1058**	**(s) 1058**	**(m) 1058**	**(w) 1057**	**(m) 1058**	**(w) 1058**	–	–
mid–range luminescence effects												
–	–	–	–	–	l(m)1495	l(w) 1496	–	–	l(m) 1502	l(m) 1495	l(m) 1501	l(m) 1496
–	–	–	–	–	l(m)1727	l(m) 1726	–	–	l(m) 1724	l(m) 1726	l(m) 1723	l(m) 1728
l(w) 1755	–	l(w) 1755	l(w) 1756	l(w) 1756	l(m)1756	l(m) 1756	l(w) 1756	l(m) 1756	l(m) 1755	l(m) 1802	l(m) 1803	l(m) 1792
l(w) 1773	l(w) 1774	l(w) 1774	l(w) 1774	l(w) 1774	l(m)1774	l(m) 1774	l(w) 1774	l(w) 1774	l(m) 1774	l(m) 2093	–	–
	l(w) 1794	–	–	–	l(m)1795	l(m) 1795	l(w) 1795	l(w) 1795	l(m) 1795	–	–	–
l(w) 1924	l(w) 1926	l(w) 1927	l(w) 1926	l(w) 1929	l(m)1926	l(w) 1924	l(w) 1925	l(m) 1924	l(m) 1923	–	–	–
l(m) 2019	l(m) 2020	l(w) 2020	l(w) 2020	l(w) 2019	l(m)2020	l(m) 2020	l(m)2019	l(m) 2021	l(m) 2021	–	–	–
l(w) 2155	l(m) 2156	l(w) 2156	l(w) 2154	–	–	–	–	l(m) 2158	l(m) 2156	–	–	l(m) 2070
l(w) 2204	l(m) 2203	l(w) 2203	l(w) 2204	l(w) 2202	l(m)2156	l(m) 2156	l(m)2157	–	–	–	–	–
–	–	–	–	–	l,sh(m)2426	l,sh(w)2427	l(m)2203	l(m) 2202	–	–	–	–
l(w) 2492	l(w) 2493	l(w) 2493	l(w) 2493	l(w) 2494	l(w) 2493	l(w) 2494	l(w) 2493	l(m) 2493	l,sh(w)2419	–	l,sh(m)2440	l(m) 2437
l(w) 2578	–	–	–	–	l,sh(m)2513	l,sh(s)2513	–	–	l,sh(m)2509	–	l,sh(m)2520	l(m) 2519
l(m) 2649	l(m)2650	l(w) 2649	l(w) 2649	l(m) 2649	l(vs) 2650	l(vs) 2650	l(m)2650	l(s) 2650	l(vs) 2649	l(vs) 2647	l(vs) 2641	l(vs) 2644
–	–	–	–	–	l(m) 2791	l,sh(w)2790	l(w) 2837	–	l,sh(w)2808	–	l,sh(s)2751	l(m) 2805
high–range luminescence effects												
l(s) 3232	l(s) 3234	l(s) 3233	l(m)3234	l(s) 3234	l(s) 3235	l(s) 3234	l(s) 3234	l(vs) 3234	l(s) 3234	l(w) 3232	–	–
l(s) 3256	l(s) 3257	l(s) 3257	l(m)3257	l(s) 3258	l(s) 3258	l(s) 3258	l(s) 3257	l(vs) 3258	l(s) 3258	l(w) 3259	–	–
–	–	–	l(m)3303	–	–	–	–	–	–	–	–	–
l(m) 3323	–	l(m)3323	l(m)3325	l(m)3325	l(m) 3324	l(m) 3324	l(m)3323	l(s) 3323	l(m)3323	–	–	–
l(m) 3345	l(s) 3344	l(m)3345	l(m)3345	l(m)3344	l(s) 3344	l(m) 3344	l(m)3345	l(s) 3346	l(m)3344	–	–	–
l(m) 3423	l(s) 3422	l(m)3422	l(s) 3423	l(s) 3423	l(s) 3423	l(s) 3423	l(s) 3423	l(s) 3419	l(s) 3424	l(w) 3424	–	–
l(s) 3465	l(s) 3466	l(s) 3466	l(m)3466	l(s) 3466	l(vs) 3466	l(s) 3466	l(s) 3466	l(s) 3466	l(s) 3466	l(w) 3465	–	–

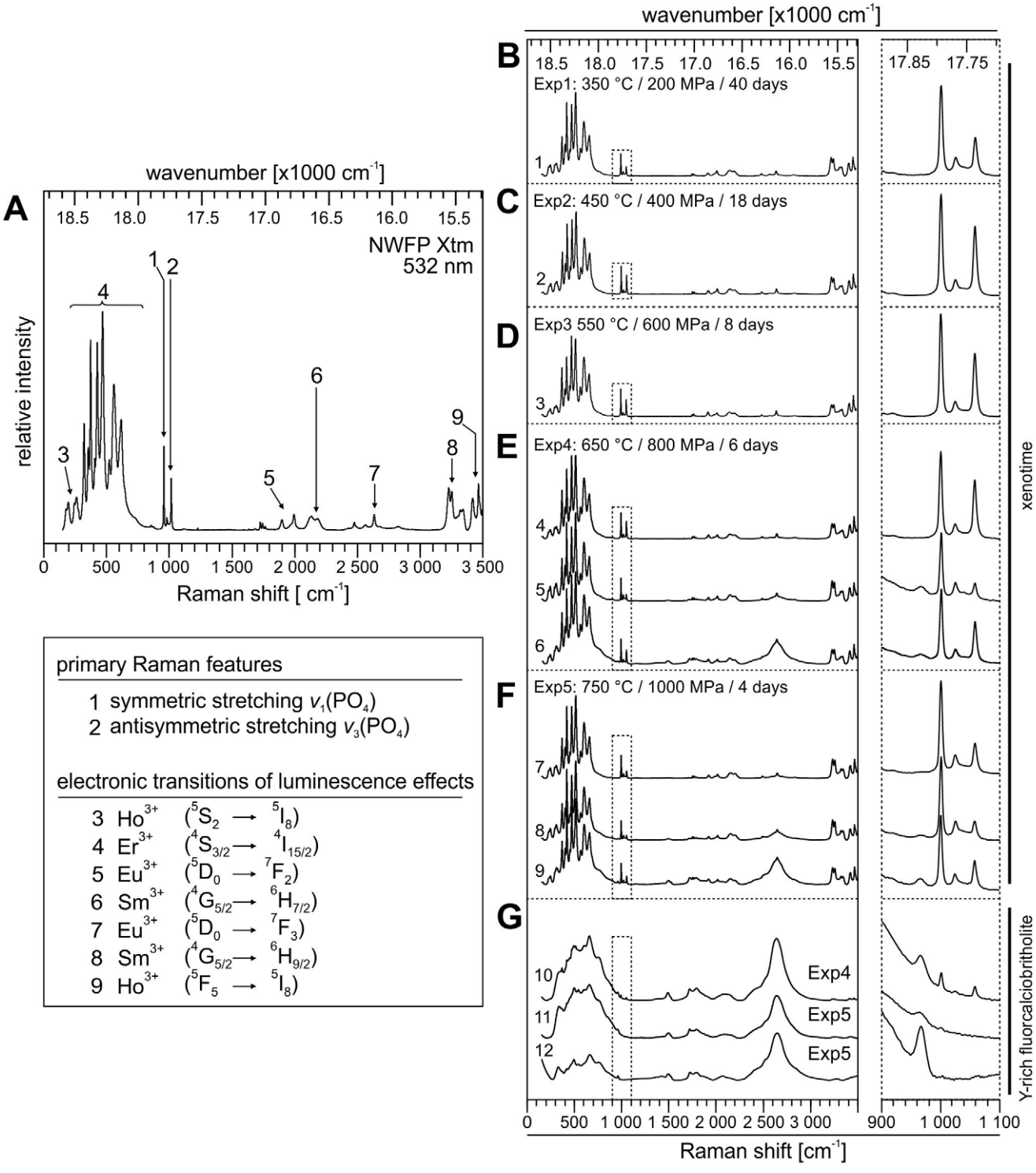

Fig. 8. Raman data of (**A**) NWFP xenotime-(Y), (**B**–**F**) xenotime-(Y) from experimental products (Exp1–Exp5) and (**G**) Y-rich fluorcalciobritholite from experimental product (Exp4 and Exp5). Right side – zoomed-in spectra (900–1100 cm^{-1}) corresponding to dotted rectangles.

Notes to Table 7:

(1) – data collected with instrument A corresponding to spectra in Figure 8 and corresponding Raman spots in Figure S3.

In bold – Raman bands; l – luminescence bands; sh – shoulders.

Xenotime-(Y) spectra: intensities of presented data are normalised to $\nu_1(PO_4)$ band equal to 1.0: weak (w) 0.05–0.2, medium (m) 0.2–0.5, strong (s) 0.5–1.0, very strong (vs) >1.0.

Y-rich fluorcalciobritholite spectra: intensities of data are normalised to characteristic Raman band (966–970 cm-1) equal to 1.0: weak (w) 0.5–1.0, medium (m) 1.0–5.0, strong (s) 5.0–10.0, very strong (vs) >10.0. Only significant signals above background are presented.

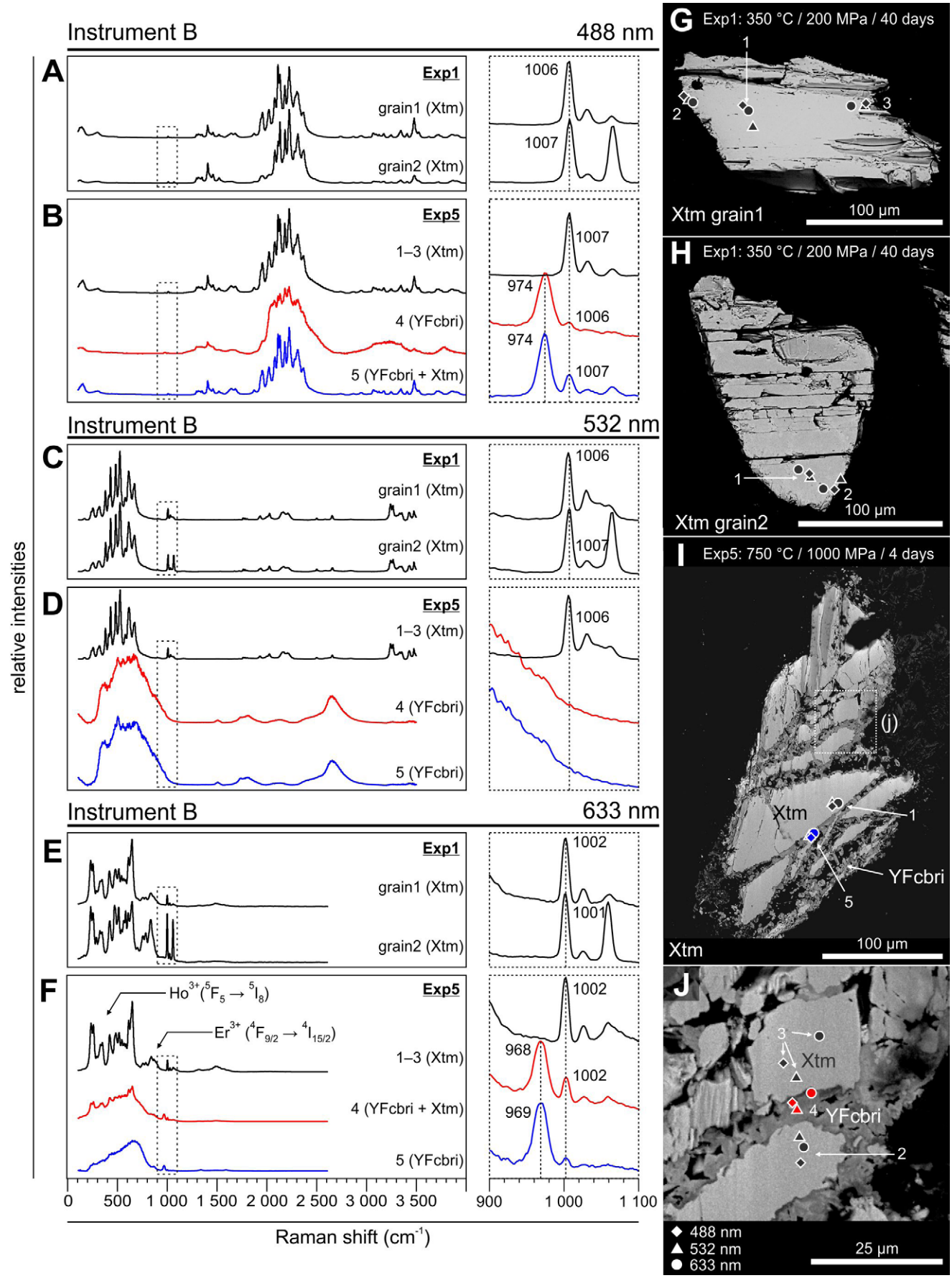

Fig. 9. Raman spectra of selected xenotime-(Y) grains from Exp1 and Exp5 collected with instrument B. **A**, **B**. 488 nm. **D**, **E**. 532 nm. **E**, **F**. 633 nm. Right side – zoomed-in spectra (900–1100 cm^{-1}) corresponding to dotted rectangles. **G**–**J**. BSE images with Raman spots. Diamond – 488 nm, triangle – 532 nm, circle – 633 nm. **F**. Electronic transitions attributed to luminescence effects taken from Lenz *et al.* (2015). Mineral abbreviations: YFcbri – Y-rich fluorcalciobritholite, Xtm – xenotime-(Y).

Compositional and Raman characteristics of the Piława Górna xenotime-(Y) – instrument A (532 nm laser)

The PG xenotime-(Y) spectra of the core and "outer" domain (i.e., opposite to the phase boundary with the zircon; Fig. 10A, B), predominantly resemble those of NWFP xenotime-(Y) and xenotime-(Y) from experiments (Figs 8, 10D). This includes the described luminescence effects of low-range luminescence effects (Ho^{3+} and Er^{3+}: $^5S_2 \rightarrow {}^5I_8$ and $^4S_{5/2} \rightarrow {}^4I_{15/2}$), weak mid-range luminescence effects (Sm^{3+}: $^4G_{5/2} \rightarrow {}^6H_{7/2}$) and high-range luminescence effects (Sm^{3+} and Ho^{3+}: $^4G_{5/2} \rightarrow {}^6H_{9/2}$ and $^5F_5 \rightarrow {}^5I_8$). However, the luminescence effects of Eu^{3+} at 1800–2000 cm^{-1}, which are present in the spectra of NWFP xenotime-(Y), are missing in the spectra of PG xenotime-(Y) (Figs 8A, 10D). One PG xenotime-(Y) spectrum from the outer domain displays broad luminescence effects in the range of 1200–1700 cm^{-1} (spectrum 2 in Fig. 10D). Xenotime-(Y) spectra from the microporous domain display increased background luminescence at 1200–1700 cm^{-1} compared to xenotime-(Y) from experiments (spectra 3, 4 in Fig. 10D). The FWHM values of the $v_1(PO_4)$ band of the outer domain (7.3–8.5 cm^{-1}), and from the microporous domain (8.5–9.0 cm^{-1}) of PG xenotime-(Y) are significantly higher than FWHM values of xenotime-(Y) from experiments (4.56–6.3 cm^{-1}; Fig. 10E).

Hyperspectral maps of xenotime-(Y) – instrument B (532 nm and 633 nm lasers)

Hyperspectral maps were collected on xenotime-(Y) grains surrounded by secondary Y-rich fluorcalciobritholite (Exp5, 1000 MPa / 750 °C; Fig. 11A). The TCA images of xenotime-(Y) (532 nm and 633 nm) demonstrate correlation with the BSE image, though not as good as the ones of monazite-(Ce) (Figs 6C, D, 11B, C). Xenotime-(Y) and Y-rich fluorcalciobritholite demonstrate sharp and distinct boundaries in the BSE image, whereas a gradual shift from xenotime-(Y) to Y-rich fluorcalciobritholite is present in the TCA image taken with the 633 nm laser (Fig. 11A, D). Even small but distinct spectral differences can be used to investigate the presence and distribution of individual phases, thus, signals of the $v_1(PO_4)$ band (1005 cm^{-1}) and luminescence effects at ca. 3250 cm^{-1} (caused by Sm^{3+} $^4G_{5/2} \rightarrow {}^6H_{9/2}$) are representative for xenotime-(Y) (Fig. 11E, H), whereas signals of the luminescence effects at 1500 cm^{-1} and 2650 cm^{-1} (caused by Eu^{3+} $^5D_0 \rightarrow {}^7F_3$) correspond to the presence of Y-rich fluorcalciobritholite (Fig. 11F, G). The distribution of these signals roughly reflects the dominant centres of both phases and fits the TCA and BSE images.

Both hyperspectral maps (532 nm and 633 nm) indicate underlying signals of Y-rich fluorcalciobritholite at the same location where the BSE image shows a homogeneous surface of xenotime-(Y) and a sharp boundary to Y-rich fluorcalciobritholite (green dashed squares in Fig. 11A, C, D). The EPMA-WDS compositional maps from the same area as the hyperspectral maps, confirm the homogeneous surface of xenotime-(Y) and sharp boundaries between xenotime-(Y) and Y-rich fluorcalciobritholite (Fig. 12).

DISCUSSION

Characteristics of the Raman spectrum of monazite-(Ce)

The unambiguous attribution of Raman bands to vibrational modes of individual symmetry is still controversial, even for pure end-members of REE phosphates, and would require *ab initio* quantum calculations (Ruschel *et al.,* 2012). Thus, the identification of Raman bands of natural monazite-(Ce) is based on Raman data of synthetic end-members of REE phosphates from this study and the literature (Tabs 3, 5; Begun *et al.,* 1981; Silva *et al.,* 2006). The predominant Ce content (0.412–0.483 apfu, Supplementary Tab. S3) in Burnet monazite-(Ce) would suggest Raman data like that of $CePO_4$. However, amongst the normal modes [$v_1(PO_4)$, $v_2(PO_4)$, $v_3(PO_4)$ and $v_4(PO_4)$], only the symmetric bending mode $v_2(PO_4)$ at 464 cm^{-1} fits best with the band position of $CePO_4$ (465 cm^{-1}; Tabs 3, 5). The other normal modes are shifted towards higher values and best-fit $NdPO_4$ [$v_1(PO_4)$ at 974 cm^{-1} and $v_4(PO_4)$ at 625 cm^{-1}] and $GdPO_4$ [$v_3(PO_4)$ at 1070 cm^{-1}], which is related to the cumulative contribution of LREE (La–Gd) to the gross structure of natural monazite-(Ce). The correlation of band position with specific REE content was shown in synthetic $Ce_{0.5}Sm_{0.5}PO_4$ or $La_{1-x}Eu_xPO_4$, in which the band positions shifted, depending on REE occupancy (Ruschel *et al.,* 2012; Geisler *et al.,* 2016). This cumulated contribution may also explain the appearance of shoulder bands at ca. 961 cm^{-1}, which could be related to the bonding length of $LaPO_4$ [$v_1(PO_4)$ at 965 cm^{-1}] and $CePO_4$ [$v_1(PO_4)$ at 968 cm^{-1}; Tab. 3].

Monazite-(Ce) can accumulate significant amounts of radiation damage leading to distortion of its structure, which is reflected in broadening of the $v_1(PO_4)$ band, despite the resistance of the mineral towards radiation damage due to low-temperature annealing effects (Seydoux-Guillaume *et al.,* 2002a, b, c, 2018; Ruschel *et al.,* 2012; Grand'Homme *et al.,* 2018; Nasdala *et al.,* 2020; Budzyń *et al.,* 2021, 2022). Raman data of unaltered and compositionally altered domains of monazite-(Ce) provide useful information in terms of structural recovery based on band narrowing (decrease of FWHM values), which is caused by recrystallization via fluid-induced coupled dissolution-reprecipitation processes (Putnis, 2002, 2009; Harlov *et al.,* 2011; Seydoux-Guillaume *et al.,* 2012) or thermal annealing (Meldrum and Boatner, 1997; Ruschel *et al.,* 2012; Seydoux-Guillaume *et al.,* 2012, 2018; Nasdala *et al.,* 2020). The correlation of FWHM with structural damage or recovery was documented for a large variety of randomly oriented samples (Ruschel *et al.,* 2012). Broadening of the $v_1(PO_4)$ symmetric stretching band is caused (i) by chemical broadening (structural distortion when incorporating U, Th, Ca and Pb in the monazite-(Ce) lattice) and (ii) by radiation damage (Ruschel *et al.,* 2012). The high FWHM values (12.2–15.9 cm^{-1}) of Burnet monazite-(Ce) compared to chemical broadening (7.2–8.7 cm^{-1}) indicates a moderate degree of structural disorder caused by an accumulation of radiation damage (Fig. 3A).

Altered domains of monazite-(Ce) grains from experimental products at low to moderate P-T conditions (Expl–Exp3: 200 MPa / 350 °C, 400 MPa / 450 °C, 600 MPa / 550 °C) contain low FWHM values, which

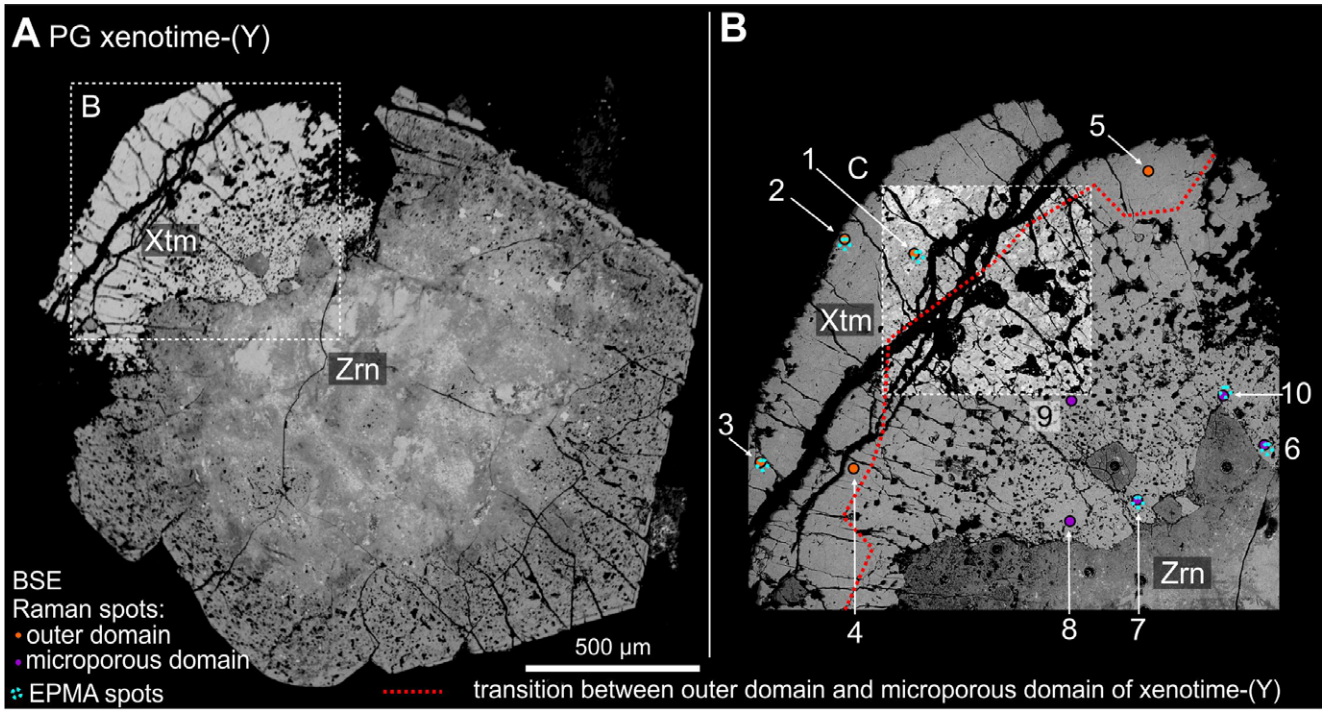

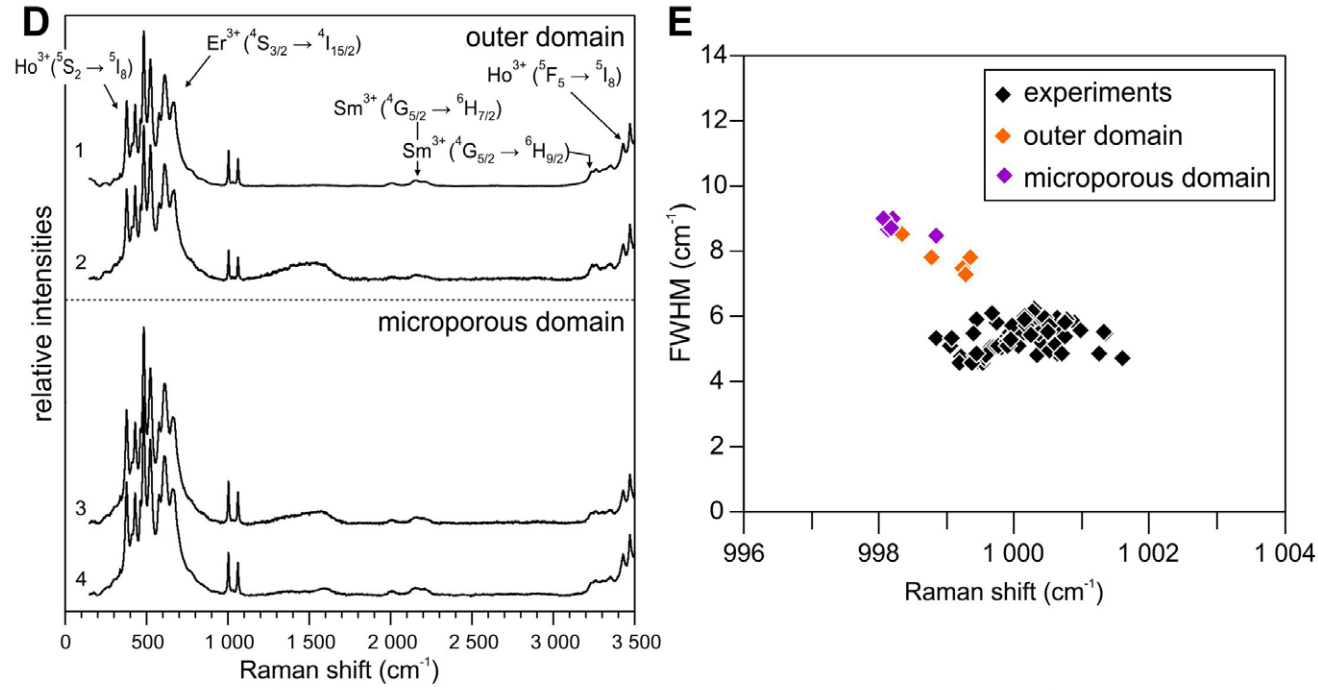

Raman spectra and corresponding Raman spots			
outer domain		microporous domain	
spectrum 1 (n = 4)	1, 2, 4, 5	spectrum 3 (n = 2)	6, 8
spectrum 2 (n = 1)	3	spectrum 4 (n = 3)	7, 9, 10

Fig. 10. BSE images and Raman data of the PG xenotime-(Y) from a pegmatite from Piława Górna (NE Bohemian Massif, SW Poland) with Raman and EPMA spots. **A**. Overview of the xenotime-(Y) and zircon. **B**. Zoomed-in image with measured spots and (**C**) High contrast BSE image demonstrating patchy zoning of xenotime-(Y) (modified from Budzyń *et al.,* 2018; Tramm *et al.,* 2021). **D**. Xenotime-(Y) spectra from the "outer domain" and patchy microporous domain. **E**. Raman shift of $\nu_1(PO_4)$ symmetric stretching band of the PG xenotime-(Y) and xenotime-(Y) from experiments vs. corresponding FWHM values. See text for details.

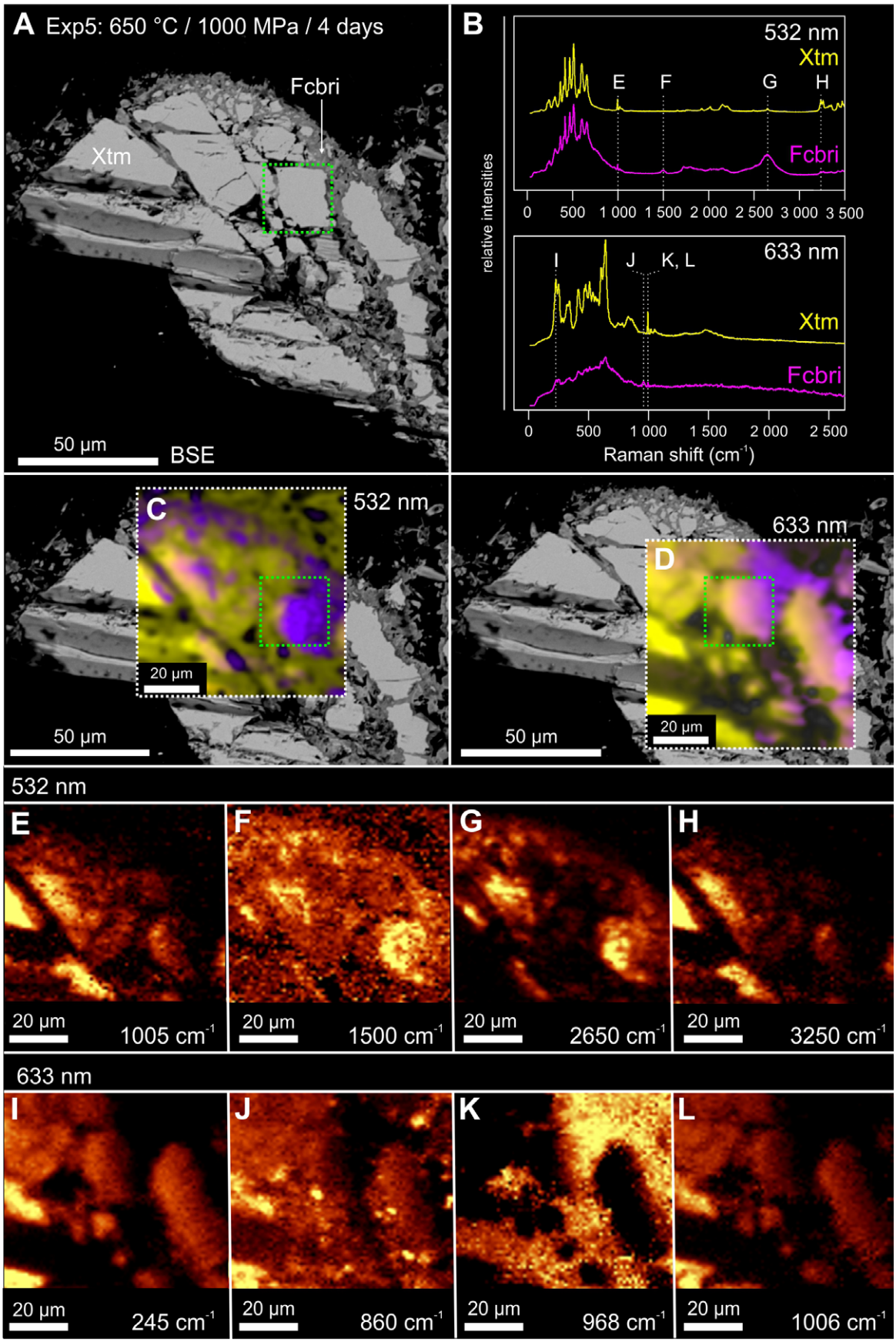

Fig. 11. Hyperspectral maps (instrument B) of xenotime-(Y) from Exp5 (1000 MPa / 750 °C). **A**. BSE overview and selected area. **B**. Raman spectra and (**C**, **D**) TCA images of xenotime-(Y) and Y-rich fluorcalciobritholite obtained with 532 nm and 633 nm lasers. **E**–**H**. Intensity maps of distinct bands (532 nm). **I**–**L**. Intensity maps of selected distinct bands (633 nm). A, C, D – green dashed square – highlighted area corresponding to the same position in BSE image and hyperspectral maps. Mineral abbreviations: YFcbri – Y-rich fluorcalciobritholite, Xtm – xenotime-(Y).

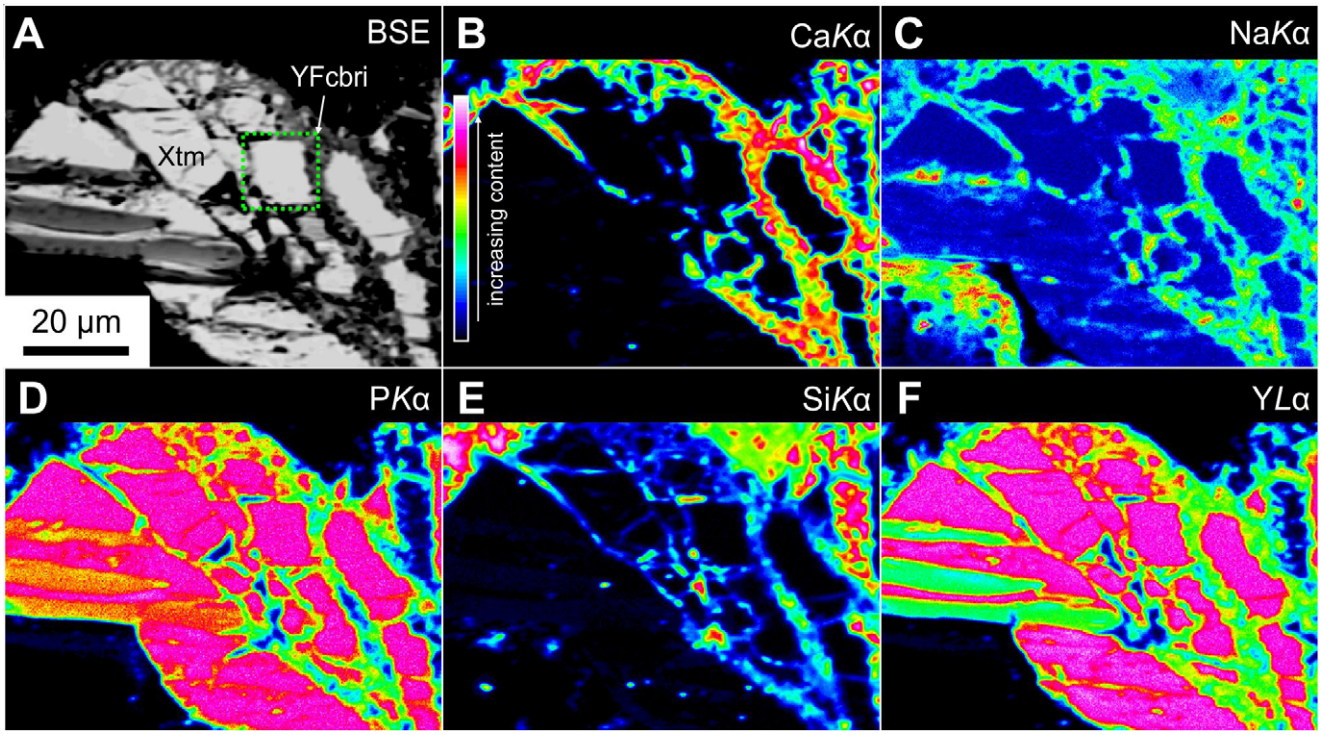

Fig. 12. BSE image and EPMA-WDS compositional X-ray maps of a selected area of xenotime-(Y) from Exp5 (1000 MPa / 750 °C). Green dashed square – location of interest from the hyperspectral map (green dashed square in Fig. 11A, C, D). Mineral abbreviations: YFcbri – Y-rich fluorcalciobritholite, Xtm – xenotime-(Y).

reflect recrystallisation due to coupled dissolution-reprecipitation processes. The alkaline fluids used in experiments mobilised U, Th, Pb and HREE (Fig. 3B–D; Supplementary Fig. S2; Tab. S3; cf. Budzyń *et al.,* 2015, 2017, 2021). On the other hand, higher FWHM values of unaltered monazite-(Ce) domains indicate a moderate disorder of the structure, which was retained during experiments. The overall Raman data of unaltered domains (Exp1–Exp5, 200–1000 MPa / 350–750 °C) display a general trend of decreasing FWHM, which indicates partial structural recovery interpreted to be caused by progressively increasing contribution of thermal annealing (Fig. 3B–D; cf. Ruschel *et al.,* 2012; Seydoux-Guillaume *et al.,* 2012, 2018; Nasdala *et al.,* 2020; Budzyń *et al.,* 2021, 2022).

A contradictory observation is that a large fraction of data (altered domains in Exp1–Exp3, and unaltered domains in Exp4–Exp5) display lower values of the Raman shift than the chemical broadening suggests. These may be the result of combined factors: (i) overcorrection of small FWHM values, a flaw of the correction method applied for instrumental broadening (e.g., Irmer, 1985; Nasdala *et al.,* 2001), and (ii) overestimation of chemical broadening. Altered domains are classified by textural evidence, such as microporosity, presence of secondary phases and depletion of Th, U and Pb. The presence of secondary micro- to submicron-inclusions is a common result of coupled dissolution-reprecipitation processes (Putnis, 2002, 2009; Harlov *et al.,* 2011; Seydoux-Guillaume *et al.,* 2012), thus, chemical broadening may be overestimated in the altered domains of monazite-(Ce).

In the case of unaltered domains from experiments at higher temperatures (Exp4–Exp5), calculated chemical broadening is significantly higher than that of Burnet monazite-(Ce) [up to 9.4 cm^{-1} in Exp4 or 10.2 cm^{-1} in Exp5, compared to 8.7 cm^{-1} in Burnet monazite-(Ce)]. The experiments were carried out under high bulk Ca and Na conditions (Budzyń *et al.,* 2017). Therefore, it is possible that some Ca in monazite-(Ce) was supplied by the fluid during alteration at the submicron scale without significantly affecting the overall composition. Possibly, nanoinclusions of cheralite [$CaTh(PO_4)_2$] in nanopores have formed and are distributed over the entire monazite-(Ce) grain, similarly to secondary cheralite nanoinclusions observed with TEM in monazite-(Ce) from the same experiments, but at P-T conditions 200 MPa / 750 °C (Budzyń *et al.,* 2021). Therefore, the low FWHM values of most data, even below calculated chemical broadening, from Exp4 and Exp5 may be the result of overlapping processes, such as thermal annealing and submicron fluid-induced alteration processes. Confirmation of such interpretation, however, would require nanoscale analyses (e.g., TEM) of the investigated grains, which was outside of the scope of this work.

The Raman data of compositionally unaltered monazite-(Ce) from Exp2 (400 MPa / 450 °C) show significant changes, compared to that of the Burnet monazite-(Ce) at two locations close to REE-rich steacyite (spots 50, 51 in Supplementary Fig. S1H; spectrum 15 in Fig. 2G). Monazite-(Ce) spectrum 15 contains a distinct band at 1128 cm^{-1} and significantly increased mid-range luminescence effects are present (Fig. 2G). The proximity of the secondary REE-rich steacyite suggests the potential contribution of this phase in the monazite-(Ce) spectrum. Jin and Soderholm (2015) studied Raman spectra of synthetic minerals similar to steacyite [(K,□)

$(Na,Ca)_2(Th,U)Si_8O_{20}$] (Perrault and Szymański, 1982), i.e., $(Ca_{0.5}Na_{0.5})_2NaUSi_8O_{20}$ and $(Ca_{0.5}Na_{0.5})_2NaThSi_8O_{20}$. The spectra of these minerals include a band at a similar position [1144 cm^{-1} in $(Ca_{0.5}Na_{0.5})_2NaUSi_8O_{20}$ and 1139 cm^{-1} $(Ca_{0.5}Na_{0.5})_2NaThSi_8O_{20}$, respectively] as observed in the monazite-(Ce) spectrum collected closely to REE-rich steacyite (1128 cm^{-1}). These bands were attributed to the antisymmetric stretching of the Si-O-Si bond (Jin and Soderholm, 2015), thus, the additional distinct band at 1128 cm^{-1} observed in the monazite-(Ce) spectrum may suggest a contribution of antisymmetric stretching of the Si-O-Si bond of REE-rich steacyite or possibly a similar phase. However, this interpretation remains uncertain due to the lack of reference spectra and emphasises that the Raman database should be expanded for not evaluated phases (spectrum 15 in Fig. 2G).

Some Raman spectra obtained from compositionally unaltered monazite-(Ce) domains (Exp5, 1000 MPa / 750 °C), but close to secondary fluorcalciobritholite, display significant spectral changes compared to that of the Burnet monazite-(Ce) (Raman spots 99, 111, 134; EPMA spots 72, 83, 92 in Supplementary Fig. S1S, U, W). The spectral characteristics include the appearance of a distinct band at 860 cm^{-1} and an increase of luminescence effects at mid- and high-range (spectra 19, 20 in Fig. 2J), which are similar to spectra of fluorcalciobritholite (spectra 23–25 in Fig. 2K). Signals of fluorcalciobritholite in Raman spectra of monazite-(Ce) may be used to identify its presence based on the distinct Raman features, which include a shifted $\nu_1(PO_4)$ band towards lower wavenumbers (ca. 960–965 cm^{-1}), the appearance of a new band at ca. 860 cm^{-1} and increased luminescence effects at mid- and high-range in accordance to fluorcalciobritholite reference spectra. A mixture of fluorcalciobritholite with other britholite-group minerals cannot be excluded from the spectra due to the formation of many small crystals. Detailed textural and compositional descriptions of secondary phases from the investigated products of experiments were previously completed (Budzyń *et al.*, 2017) indicating fluorcalciobritholite as the predominant secondary phase at the P-T conditions selected in this work, thus, reference spectra are attributed to predominantly reflect fluorcalciobritholite further on if not stated otherwise.

Two Raman spectra collected very closely to micropores filled with fluorcalciobritholite display predominantly signals of fluorcalciobritholite over signals of monazite-(Ce) (spectra 17, 18 in Fig. 2H, I; Raman spots 56, 69, 70, 82 in Supplementary Fig. S1I, N, Q). The contribution of fluorcalciobritholite signals to the monazite-(Ce) spectra could be related to (i) the formation of submicron inclusions of fluorcalciobritholite in the monazite-(Ce) matrix, or (ii) the presence of a phase boundary beneath the sample surface. This interpretation further supports the discussion above about the observed low FWHM values for a large fraction of monazite-(Ce) data from Exp5 and suggests submicron alteration processes without significantly changing the chemical composition. Furthermore, nanoinclusions of britholite have been documented with TEM in experimentally altered monazite-(Ce) at high temperatures (1000 MPa / 900 °C; Harlov *et al.,* 2011). Thus, the presence of fluorcalciobritholite submicron inclusions is plausible.

Characteristics of the Raman spectrum of xenotime-(Y)

In contrast to the Burnet monazite-(Ce), the Raman bands of the NWFP xenotime-(Y) are located at the expected positions of its composition (0.72–0.76 apfu Y) and fit well with data of YPO_4 (1B [$\nu_1(PO_4)$] = 999 cm^{-1}, 2B = 1024 cm^{-1} and 3B [$\nu_3(PO_4)$] = 1056 cm^{-1}; Tabs 4, 7). This implies that either (i) the monazite-(Ce) structure and the positions of vibrational modes are more susceptible to REE composition than the xenotime-(Y) structure, or (ii) that the Y content in the xenotime-(Y) structure exceeded a threshold, which results in a structure reflecting that of YPO_4. The Raman spectrum of NWFP xenotime-(Y) in this work shows low-range luminescence effects caused by the Ho^{3+} ($^5S_2 \rightarrow {}^5I_8$) and Er^{3+} ($^4S_{3/2} \rightarrow {}^4I_{15/2}$), which superimpose the lattice and internal bending modes of xenotime-(Y) and electronic transitions derived from Dieke diagrams (Dieke and Crosswhite, 1963) and agree with observations of Lenz *et al.* (2015) of xenotime-(Y) spectra from Novo Horizonte (Baha, Brazil).

The similarity of most xenotime-(Y) spectra from all experiments reflects its chemical and structural stability (spectra 1–4, 7 in Fig. 8B–F). Still, there is textural evidence for alteration in BSE images of xenotime-(Y) from Exp4 and Exp5 (800 MPa / 650°C, 1000 MPa / 750 °C), which includes dissolution pits at the rim of xenotime-(Y) and partial replacement of xenotime-(Y) by Y-rich fluorcalciobritholite (Supplementary Fig. S3I–L). Indeed, some Raman spectra collected at the very rim of xenotime-(Y) grains close to Y-rich fluorcalciobritholite show characteristic changes in luminescence effects (spectra 6, 8, 9 in Fig. 8E, F). Particularly the dominant Eu^{3+} ($^5D_0 \rightarrow {}^7F_3$) luminescence band at ca. 2650 cm^{-1}, which demonstrates increased intensity and broadening, resembles those of Y-rich fluorcalciobritholite (spectra 6, 9 and 10–12 in Fig. 8E–G). Other luminescence bands at ca. 1900 and 2000 cm^{-1} caused by different electronic transitions of Eu^{3+} ($^5D_0 \rightarrow {}^7F_2$) display broadening (Fig. 8E, F). This phenomenon may indicate that structural changes can affect individual electronic transitions of one REE (in this case Eu^{3+}) or that individual electronic transitions of one REE are activated differently depending on crystal orientation. Indeed, a different response of the Raman spectrum on crystal orientation was demonstrated in $PrPO_4$ with polarised Raman spectroscopy (Silva *et al.,* 2006).

Raman microspectroscopy of the Ankazobe monazite-(Ce) and the Piława Górna xenotime-(Y)

Unaltered domains of the Ankazobe monazite-(Ce) display significant broadening of the $\nu_1(PO_4)$ band (10.5–13.2 cm^{-1} FWHM) at relatively constant U, Th, Ca and Pb contents, which indicate various degrees of radiation damage in the structure (Fig. 5E, Supplementary Tab. S3). In comparison, the Burnet monazite-(Ce) displays a slightly higher degree of radiation damage shown in band broadening of 12.2–15.9 cm^{-1} FWHM at higher chemical broadening (Fig. 3A). The differences in chemical broadening are due to higher Th, Pb and Ca contents in Burnet monazite-(Ce) compared to Ankazobe monazite-(Ce). However, despite their ages (Burnet monazite-(Ce), ca. 1100 Ma; Budzyń *et*

al., 2021; Ankazobe monazite-(Ce), ca. 515 Ma; Budzyń and Sláma – unpublished data), both monazites display only moderate degrees of radiation damage based on FWHM values. Because annealing effects occur at temperatures as low as 180 °C (Seydoux-Guillaume *et al.,* 2018), structural damage caused by self-irradiation was repaired as long as the environment had adequate temperature conditions. The degree of radiation damage observed in both monazites is therefore the result of accumulated structural damage after termination of annealing. This may be related to the termination of annealing processes which repaired the Burnet monazite-(Ce) structure and the Ankazobe monazite-(Ce) at different times.

Raman data from the altered domains of the Ankazobe monazite-(Ce) show significant ν_1PO_4 band narrowing (6.3–10.2 cm^{-1}; Fig. 5E) and depletion of Th, U and Pb (Supplementary Tab. S3), which indicate structural recovery due to recrystallization via fluid-aided coupled dissolution-reprecipitation processes. These observations are in agreement with earlier studies (Ruschel *et al.,* 2012; Seydoux-Guillaume *et al.,* 2012, 2018; Budzyń *et al.,* 2021, 2022), and demonstrate the value of Raman microspectroscopy in constraining degree of alteration in the altered domains.

In the case of the investigated PG xenotime-(Y) and xenotime-(Y) from experiments, correlation of U, Th, Ca and Pb contents with band broadening, as demonstrated for monazite-(Ce) (Ruschel *et al.,* 2012), was not observed (Fig. 10D; Supplementary Tab. S6). The reason for lack of such correlation is most likely related to low concentrations of U, Th, Ca and Pb in the investigated xenotime-(Y). Also, it cannot be excluded that these non-formula elements do not distort the xenotime-(Y) structure in the same way as they affect the monazite-(Ce) structure. In the NWFP xenotime-(Y), radiation damage did not accumulate sufficiently, whereas the PG xenotime-(Y) with higher contents of U, Th, Ca and Pb, and altered at high temperature conditions during pegmatite formation (Budzyń *et al.,* 2018), displays ν_1PO_4 band broadening (7.3–9.0 cm^{-1} FWHM) that indicates a moderate degree of accumulated radiation damage. For comparison, a moderate degree of radiation damage was demonstrated in a micro- to nanoscale study of xenotime-(Y) from a pegmatite (Evje, S Norway) with Raman microspectroscopy and TEM (Budzyń *et al.,* 2023b). The primary xenotime-(Y) (ca. 980 Ma) yielded high FWHM values (13.3–15.6 cm^{-1}), whereas altered domains with recrystallized structure have shown low to moderate FWHM values (1.1–9.8 cm^{-1}; Budzyń *et al.,* 2023b). The Raman data of pegmatitic xenotime-(Y) from Piława Górna and the Evje region demonstrate two cases in which Raman microspectroscopy identified domains in xenotime-(Y) with various degrees of radiation damage.

Hyperspectral maps of monazite-(Ce) and xenotime-(Y)

Hyperspectral maps of monazite-(Ce) provide information on structural variations, whilst fitting well with EPMA-WDS compositional X-ray maps and BSE images (Figs 6, 7). Structural variation is revealed by a shift of band positions of the $\nu_1(PO_4)$ band (978–962 cm^{-1}) with both excitation lasers (532 and 633 nm) and demonstrates the high potential of combining hyperspectral maps with EPMA compositional X-ray maps. The combined data provide broader information in terms of phase identification, and compositional and structural relations within phases.

Hyperspectral maps of xenotime-(Y) resulted in more ambiguous TCA images which partially contradict BSE images and EPMA-WDS compositional X-ray maps (Figs 11, 12). Signals from xenotime-(Y) and Y-rich fluorcalciobritholite are present in domains, which show homogeneous xenotime-(Y) in BSE images and compositional X-ray maps (green square; Figs 11, 12). When interpreting hyperspectral and EPMA compositional X-ray maps, the depth resolution of both methods needs consideration (Hetherington *et al.,* 2008; Everall, 2010). The depth resolution of Raman microspectroscopy can be estimated with the formula $\Delta z = 4\lambda \times NA^{-2}$ (NA = 0.45) and depends on the excitation laser used (10.5 μm depth with 532 nm and 12.5 μm depth with 633 nm; after Everall, 2010). A focused electron beam of EPMA possesses a resolution as low as 6 μm^3 when applied to xenotime-(Y) with 15 kV acceleration and a current of 200 nA (Hetherington *et al.,* 2008). In this work, an acceleration of 15 kV and a current of 100 nA were applied with a beam size of 3 μm leading to a resolution of < 6 μm^3. Thus, EPMA measurements and compositional X-ray maps reflect the imminent surface of the sample. In contrast, hyperspectral maps penetrate the material deeper and reflect the gross signal from the surface up to 12 μm into the sample. A combination of hyperspectral maps with EPMA-WDS compositional X-ray maps of xenotime-(Y) indicate that spectral signals of Y-rich fluorcalciobritholite are located below the xenotime-(Y) (green square; Figs 11, 12). This particular domain of xenotime-(Y) may be suitable for compositional evaluation with EPMA measurements, however, Raman data suggest caution regarding trace element analysis or geochronological evaluation with other microanalytical techniques such as LA-ICPMS.

CONCLUSIONS

This work systematically applied the collective knowledge of previous Raman spectroscopic works on monazite-(Ce) and xenotime-(Y) to natural and experimental cases of fluid-induced alteration to evaluate spectral changes between unaltered and altered domains. The Raman data for monazite-(Ce) and xenotime-(Y) from the laboratory experiments have distinct spectral characteristics in unaltered and altered domains, which display significant band narrowing in monazite-(Ce), in combination with U, Th and Pb depletion and enrichment of Ca, indicating recrystallized domains as a result of fluid-induced coupled dissolution-reprecipitation processes. Monazite-(Ce) demonstrated minimal compositional changes at elevated temperatures but showed a progressive decrease of the FWHM values of ν_1PO_4 bands, which is attributed to thermal annealing processes potentially coupled with submicron alteration processes. Significantly lower values of FWHM than calculated chemical broadening can be the result of Ca-bearing submicron inclusions formed in monazite-(Ce) during alteration driven by fluid-induced coupled dissolution-reprecipitation processes.

The Raman data of monazite-(Ce) and xenotime-(Y) demonstrate the importance of a structural evaluation with spectroscopic methods in petrological and petrochronological studies of altered monazite-(Ce) and xenotime-(Y). The application of hyperspectral mapping is particularly useful to complete information from EPMA-WDS X-ray mapping and to understand the presence of phases present below the analysed surface, which may affect microanalytical results. Changes in primary Raman features can easily identify signals of secondary phases in the monazite-(Ce) and xenotime-(Y) spectra, but luminescence effects are often ignored or unwanted. Yet, REE-bearing phases such as fluorcalciobritholite demonstrated significant changes in luminescence effects, thus characteristic luminescence effects prove to be a valid indicator for differentiation of unaltered and altered domains in monazite-(Ce) and xenotime-(Y), and between other REE-bearing phases.

The extended Raman dataset enables differentiation of alteration mechanisms, such as structural damage due to self-irradiation, recrystallization due to coupled dissolution-reprecipitation or thermal annealing effects, if combined with textural and compositional data, particularly with the 532 nm and 633 nm lasers. Comparison of chemical broadening and measured FWHM values of the ν_1PO_4 band of monazite-(Ce) are very useful to differentiate between radiation-damaged domains, compositionally altered and recrystallized domains, and compositionally unaffected domains, which most likely underwent a combination of thermal annealing and submicron recrystallization. Raman microspectroscopy extends our understanding of alteration processes of monazite-(Ce) and xenotime-(Y) and may bear the potential to improve Raman characterizations with other not yet evaluated excitation lasers.

Acknowledgements

I. Broska and E. Janots are thanked for valuable comments in their reviews. The Burnet monazite-(Ce) was provided by M. L. Williams and M. J. Jercinovic. The NWFP xenotime-(Y) and synthetic end-members of REE phosphates ($LaPO_4$–$LuPO_4$, YPO_4) were provided by D. E. Harlov. The authors acknowledge M. L. Williams and C. Barnes for their comments on earlier versions of this work. This study was financially supported by the Polish National Science Centre (NCN) research grant no. 2017/27/B/ST10/00813 (to B.B.). A. Uchman, E. Malata and F. Simpson are acknowledged for editorial corrections. M. Gradziński is thanked for editorial handling of the manuscript. The experimental products are from previous projects, financially supported by the Polish National Science Centre (NCN) Grant No. 2011/01/D/ST10/04588 and the IGS PAS Research Funds – Project "EXP" (to B. B.). J. S. was supported by the ASCR institutional support RVO67985831. This study represents a modified part of the PhD thesis of F. Tramm.

REFERENCES

Andrehs, G. & Heinrich, W., 1998. Experimental determination of REE distributions between monazite and xenotime: Potential for temperature-calibrated geochronology. *Chemical Geology*, 149: 83–96.

Begun, G. M., Beall, G. W., Boatner, L. A. & Gregor, W. J., 1981. Raman spectra of the rare earth orthophosphates. *Journal of Raman Spectroscopy*, 11: 273–278.

Boatner, L. A., 2002. Synthesis, structure, and properties of monazite, pretulite, and xenotime. In: Kohn, J. K. & Hughes, J. M. (eds), *Phosphates: Geochemical, Geobiological, and Materials Importance*. *Reviews in Mineralogy and Geochemistry*, 48: 87–121.

Broska, I. & Siman, P., 1998. The breakdown of monazite in the West-Carpathian Veporic orthogneisses and Tatric granites. *Geologica Carpathica*, 49: 161–167.

Broska, I., Williams, C. T., Janák, M. & Nagy, G., 2005. Alteration and breakdown of xenotime-(Y) and monazite-(Ce) in granitic rocks of the Western Carpathians, Slovakia. *Lithos*, 82: 71–83.

Budzyń, B., Harlov, D., Kozub-Budzyń, G. A. & Majka, J., 2017. Experimental constraints on the relative stabilities of the two systems monazite-(Ce) – allanite-(Ce) – fluorapatite and xenotime-(Y) – (Y,HREE)-rich epidote – (Y,HREE)-rich fluorapatite, in high Ca and Na-Ca environments under P-T conditions of 200–1000 MPa and 450–750 °C. *Mineralogy and Petrology*, 111: 183–217.

Budzyń, B., Harlov, D. E., Williams, M. L & Jercinovic, M. J., 2011. Experimental determination of stability relations between monazite, fluorapatite, allanite, and REE-epidote as a function of pressure, temperature, and fluid composition. *American Mineralogist*, 96: 1547–1567.

Budzyń, B., Hetherington, C. J., Williams, M. L. & Michalik, M., 2010. Fluid-mineral interactions and constraints on monazite alteration during metamorphism. *Mineralogical Magazine*, 74: 659–681.

Budzyń, B., Konečný, P. & Kozub-Budzyń, G. A., 2015. Stability of monazite and disturbance of the Th-U-Pb system under experimental conditions of 250–350 °C and 200–400 MPa. *Annales Societatis Geologorum Poloniae*, 85: 405–424.

Budzyń, B. & Kozub-Budzyń, G. A., 2015. The stability of xenotime in high Ca and Ca-Na systems, under experimental conditions of 250–350°C and 200–400 MPa: the implications for fluid-mediated low-temperature processes in granitic rocks. *Geological Quarterly*, 59: 316–324.

Budzyń, B. & Sláma, J., 2019. Partial resetting of U-Pb ages during experimental fluid-induced re-equilibration of xenotime. *Lithos*, 346–347: 105163.

Budzyń, B., Sláma, J., Kozub-Budzyń, G. A., Konečný, P., Holický, I., Rzepa, G. & Jastrzębski, M., 2018. Constraints on the timing of multiple thermal events and re-equilibration recorded by high-U zircon and xenotime: Case study of pegmatite from Piława Górna (Góry Sowie Block, SW Poland). *Lithos*, 310–311: 65–85.

Budzyń, B., Wirth, R., Sláma, J., Birski, Ł., Tramm, F., Kozub-Budzyń, G. A., Rzepa, G. & Schreiber, A., 2021. LA-ICPMS, TEM and Raman study of radiation damage, fluid-induced alteration and disturbance of U-Pb and Th-Pb ages in experimentally metasomatised monazite. *Chemical Geology*, 583: 120464.

Budzyń, B., Wirth, R., Sláma, J., Kozub-Budzyń, G. A., Konečný, P., Rzepa, G. & Schreiber, A., 2023b. Micro- to nanoscale constraints on metasomatic alterations of xenotime, inclusions of Th-, U- and Pb-phases and their geochronological implications (Ås pegmatite, Evje and Hornnes, S Norway). *Chemical Geology*, 632: 121538.

Budzyń, B., Wirth, R., Sláma, J., Kozub-Budzyń, G., Rzepa, G. & Schreiber, A., 2022. A detailed and comprehensive TEM, EPMA and Raman characterization of high-metamorphic grade monazites and their U-Th-Pb systematics (the Góry Sowie Block, SW Poland). *Chemical Geology*, 607: 121015.

Budzyń, B., Wirth, R., Sláma, J., Kozub-Budzyń & G. A., Schreiber, A., 2023a. Atomic-scale Th and U segregation into dislocation cores and U-Pb age discordance in xenotime. *Lithos*, 444–445: 107105.

Cherniak, D. J., 2006. Pb and rare earth element diffusion in xenotime. *Lithos*, 88: 1–14.

Cherniak, D. J., 2010. Diffusion in accessory minerals: Zircon, titanite, apatite, monazite and xenotime. In: Zhang, Y. & Cherniak, D. J. (eds), *Diffusion in Minerals and Melts. Reviews in Mineralogy and Geochemistry*, 72: 827–869.

Cherniak, D. J., Watson, E. B., Grove, M. & Harrison, T. M., 2004. Pb diffusion in monazite: A combined RBS/SIMS study. *Geochimica et Cosmochimica Acta*, 68: 829–840.

Clavier, N., Mesbah, A., Szenknect, S. & Dacheux, N., 2018. Monazite, rabdophane, xenotime & churchite: Vibrational spectroscopy of gadolinium phosphate polymorphs. *Spectrochimica Acta Part A: Molecular and Biomolecular Spectroscopy*, 205: 85–94.

Clavier, N., Podor, R. & Dacheux, N., 2011. Crystal chemistry of the monazite structure. *Journal of the European Ceramic Society*, 31: 941–976.

Didier, A., Bosse, V., Boulvais, P., Bouloton, J., Paquette, J. L., Montel, J. M. & Devidal, J. L., 2013. Disturbance versus preservation of U-Th-Pb ages in monazite during fluid-rock interaction: textural, chemical and isotopic in situ study in microgranites (Velay Dome, France). *Contributions to Mineralogy and Petrology*, 165: 1051–1072.

Dieke, G. H. & Crosswhite, H. M., 1963. Emission spectra of the doubly and triply ionized rare earths. *Journal of the Optical Society of America*, 51: 675–686.

Dijkman, F. G. & Van der Maas, J. H., 1976. Dependence of bandshape and depolarization ratio on slitwidth. *Applied Spectroscopy*, 30: 545–546.

Ende, M., Chanmuang, N. C., Reiners, P. W., Zamyatin, D. A., Gain, S. E. M., Wirth, R. & Nasdala, L., 2021. Dry annealing of radiation-damaged zircon: Single-crystal X-ray and Raman spectroscopy study. *Lithos*, 406–407: 106523.

Everall, N. J., 2010. Confocal Raman microscopy: Common errors and artefacts. *Analyst*, 135: 2512–2522.

Fielding, I. O. H., Johnson, S. P., Zi, J. W., Rasmussen, B., Dunkley, D. J., Sheppard, S., Wingate, M. T. D. & Rogers, J. R., 2017. Using in situ SHRIMP U-Pb monazite and xenotime geochronology to determine the age of orogenic gold mineralization: An example from the Paulsens Mine, Southern Pilbara Craton. *Economic Geology*, 112: 1205–1230.

Finger, F., Broska, I., Roberts, M. P. & Schermaier, A., 1998. Replacement of primary monazite by apatite-allanite-epidote coronas in an amphibolite facies granite gneiss from the eastern Alps. *American Mineralogist*, 83: 248–258.

Förster, H. J., 1998. The chemical composition of REE-Y-Th-U-rich accessory minerals from peraluminous granites of the Erzgebirge-Fichtelgebirge region, Germany. Part I: The monazite-(Ce)-brabantite solid solution series. *American Mineralogist*, 83: 259–272.

Gaft, M., Reisfeld, R. & Panczer, G., 2015. *Modern Luminescence Spectroscopy of Minerals and Materials*. Second Edition. Springer, pp. 220–221.

Geisler, T., Popa, K. & Konings, R. J. M., 2016. Evidence for Lattice Strain and Non-ideal Behavior in the $(La_{1-x}Eu_x)PO_4$ Solid Solution from X-ray Diffraction and Vibrational Spectroscopy. *Frontiers in Earth Science*, 4: 1–12.

Geisler, T., Schaltegger, U. & Tomaschek, F., 2007. Re-equilibration of zircon in aqueous fluids and melts. *Elements*, 3: 43–50.

Grand'Homme, A., Janots, E., Seydoux-Guillaume, A. M., Guillaume, D., Bosse, V. & Magnin, V., 2016. Partial resetting of the U-Th-Pb systems in experimentally altered monazite: Nanoscale evidence of incomplete replacement. *Geology*, 44: 431–434.

Grand'Homme, A., Janots, E., Seydoux-Guillaume, A. M., Guillaume, D., Magnin, V., Hövelmann, J., Höschen, C. & Boiron, M. C., 2018. Mass transport and fractionation during monazite alteration by anisotropic replacement. *Chemical Geology*, 484: 51–68.

Gratz, R. & Heinrich, W., 1997. Monazite-xenotime thermobarometry: Experimental calibration of the miscibility gap in the binary system $CePO_4$–YPO_4. *American Mineralogist*, 82: 7–8.

Harlov, D. E. & Hetherington, C. J., 2010. Partial high-grade alteration of monazite using alkali-bearing fluids: Experiment and nature. *American Mineralogist*, 95: 1105–1108.

Harlov, D. E. & Wirth, R., 2012. Experimental incorporation of Th into xenotime at middle to lower crustal P-T utilizing alkali-bearing fluids. *American Mineralogist*, 97: 641–652.

Harlov, D. E., Wirth, R. & Hetherington, C. J., 2007. The relative stability of monazite and huttonite at 300–900 °C and 200–1000 MPa: Metasomatism and the propagation of metastable mineral phases. *American Mineralogist*, 92: 1652–1664.

Harlov, D. E., Wirth, R. & Hetherington, C. J., 2011. Fluid-mediated partial alteration in monazite: the role of coupled dissolution–reprecipitation in element redistribution and mass transfer. *Contributions to Mineralogy and Petrology*, 162: 329–348.

Harrison, T. M., Catlos, E. J. & Montel, J. M., 2002. U-Th-Pb dating of phosphate minerals. In: Kohn, J. K. & Hughes, J. M. (eds), *Phosphates: Geochemical, Geobiological, and Materials Importance*. *Reviews in Mineralogy and Geochemistry*, 48: 523–558.

Hawkins, D. P. & Bowring, S. A., 1999. U-Pb monazite, xenotime and titanite geochronological constraints on the prograde to post-band metamorphic thermal history of Paleoproterozoic migmatites from the Grand Canyon, Arizona. *Contributions to Mineralogy and Petrology*, 134: 150–169.

Heinrich, W., Andrehs, G. & Franz, G., 1997. Monazite-xenotime miscibility gap thermometry. I. An empirical calibration. *Journal of Metamorphic Geology*, 15: 3–17.

Hetherington, C. J., Harlov, D. E. & Budzyń, B., 2010. Experimental initiation of dissolution-reprecipitation reactions in monazite and xenotime: The role of fluid composition. *Mineralogy and Petrology*, 99: 165–184.

Hetherington, C. J., Jercinovic, M. J., Williams, M. L. & Mahan, K., 2008. Understanding geologic processes with xenotime: Composition, chronology, and a protocol for electron microprobe microanalysis. *Chemical Geology*, 254: 133–147.

Heuser, J., Bukaemskiy, A. A., Neumeier, S., Neumann, A. & Bosbach, D., 2014. Raman and infrared spectroscopy of

monazite-type ceramics used for nuclear waste conditioning. *Progress in Nuclear Energy*, 72: 149–155.

Huminicki, D. & Hawthorne, F., 2002. The crystal chemistry of the phosphate minerals. In: Kohn, M. J., Rakovan, J. & Hughes, J. M. (eds), *Phosphates: Geochemical, Geobiological, and Materials Importance. Reviews in Mineralogy and Geochemistry*, 48: 123–254.

Irmer, G., 1985. Zum Einfluß der Apparatefunktion auf die Bestimmung von Streuquerschnitten und Lebensdauern aus optischen Phononenspektren. *Experimentelle Technik der Physik*, 33: 501–506.

Jian, W., Mao, J., Lehmann, B., Wu, S., Chen, L., Song, S. & Xu, J., 2024. Two discrete gold mineralization events recorded by hydrothermal xenotime and monazite, Xiaoqinling gold district, central China. *American Mineralogist*, 109: 73–86.

Jin, G. B. & Soderholm, L., 2015. Solid-state syntheses and single-crystal characterizations of three tetravalent thorium and uranium silicates. *Journal of Solid State Chemistry*, 221: 405–410.

Joseph, C., Fougerouse, D., Saxey, D. W., Verberne, R., Reddy, S. M. & Rickard, W. D. A., 2021. Xenotime at the nanoscale: U-Pb geochronology and optimisation of analyses by atom probe tomography. *Geostandards and Geoanalytical Research*, 45: 443–456.

Kingsbury, J. A., Miller, C. F., Wooden, J. L. & Harrison, T. M., 1993. Monazite paragenesis and U-Pb systematics in rocks of the eastern Mojave Desert, California, U.S.A.: Implications for thermochronometry. *Chemical Geology*, 110: 147–167.

Kylander-Clark, A. R. C., 2017. Petrochronology by laser-ablation inductively coupled plasma mass spectrometry. In: Kohn, M. J., Engi, M. & Lanari, P. (eds), *Petrochronology: Methods and Applications*. *Reviews in Mineralogy and Geochemistry*, 83: 183–198.

Lalla, E. A., Shkolyar, S., Gilmour, C. M., Lozano-Gorrín, A. D., Konstantinidis, M., Freemantle, J. & Daly, M. G., 2021. Structural and vibrational analyses of $CePO_4$ synthetic monazite samples under an optimized precipitation process. *Journal of Molecular Structure*, 1223: 129150.

Lenz, C., Nasdala, L., Talla, D., Hauzenberger, C., Seitz, R. & Kolitsch, U., 2015. Laser-induced REE^{3+} photoluminescence of selected accessory minerals – An "advantageous artefact" in Raman spectroscopy. *Chemical Geology*, 415: 1–16.

Lenz, C., Talla, D., Ruschel, K., Škoda, R., Götze, J. & Nasdala, L., 2013. Factors affecting the Nd^{3+} (REE^{3+}) luminescence of minerals. *Mineralogy and Petrology*, 107: 415–428.

Macdonald, R., Bagiński, B. & Zozulya, D., 2017. Differing responses of zircon, chevkinite-(Ce), monazite-(Ce) and fergusonite-(Y) to hydrothermal alteration: Evidence from the Keivy alkaline province, Kola Peninsula, Russia. *Mineralogy and Petrology*, 111: 523–545.

McNaughton, N. J. & Rasmussen, B., 2018. Geochemical characterisation of xenotime formation environments using U-Th. *Chemical Geology*, 484: 109–119.

Meldrum, A. & Boatner, L. A., 1997. Displacive radiation effects in the monazite- and zircon-structure orthophosphates. *Physical Review B – Condensed Matter and Materials Physics*, 56: 13805–13814.

Mullica, D. F., Sappenfield, E. L. & Boatner, L. A., 1996. Monazite- and zircon-type structures of seven mixed $(Ln/Ln)PO_4$ compounds. *Inorganica Chimica*, 244: 247–252.

Nasdala, L., Akhmadaliev, S., Artac, A., Chanmuang, C., Habler, G. & Lenz, C., 2018. Irradiation effects in monazite-(Ce) and zircon: Raman and photoluminescence study of Au-irradiated FIB foils. *Physics and Chemistry of Minerals*, 45: 855–871.

Nasdala, L., Akhmadaliev, S., Burakov, B. E., Chanmuang, C. & Škoda, R., 2020. The absence of metamictization in natural monazite. *Scientific Reports*, 10: 1–9.

Nasdala, L., Pidgeon, R. T., Wolf, D. & Irmer, G., 1998. Metamictization and U-Pb isotopic discordance in single zircons: A combined Raman microprobe and SHRIMP ion probe study. *Mineralogy and Petrology*, 62: 1–27.

Nasdala, L., Wenzel, M., Vavra, G., Irmer, G., Wenzel, T. & Kober, B., 2001. Metamictization of natural zircon: Accumulation versus thermal annealing of radioactivity-induced damage. *Contributions to Mineralogy and Petrology*, 141: 125–144.

Ni, Y., Hughes, J. M. & Mariano, A. N., 1995. Crystal chemistry of the monazite and xenotime structures. *American Mineralogist*, 80: 21–26.

Perrault, G. & Szymański, J. T., 1982. Steacyite, a new name, and a re-evaluation of the nomenclature of "ekanite"-group minerals. *The Canadian Mineralogist*, 20: 59–63.

Putnis, A., 2002. Mineral replacement reactions: from macroscopic observations to microscopic mechanisms. *Mineralogical Magazine*, 66: 689–708.

Putnis, A., 2009. Mineral replacement reactions. In: Oelkers, E. H. & Schott, J. (eds), *Thermodynamics and Kinetics of Water-Rock Interaction*. *Reviews in Mineralogy and Geochemistry*, 70: 87–124.

Putnis, A. & Austrheim, H., 2010. Fluid-induced processes: metasomatism and metamorphism. *Geofluids*, 10: 254–269.

Putnis, A. & Austrheim, H., 2013. Mechanisms of Metasomatism and Metamorphism on the Local Mineral Scale: The Role of Dissolution-Reprecipitation During Mineral Re-equilibration. In: Harlov, D. E. & Austrheim, H. (eds), *Metasomatism and the Chemical Transformation of Rock, Lecture Notes in Earth System Sciences.* Springer-Verlag, Berlin, Heidelberg, pp. 141–170.

Pyle, J. M. & Spear, F. S., 2000. An empirical garnet (YAG) – xenotime thermometer. *Contributions to Mineralogy and Petrology*, 138: 51–58.

Pyle, J. M., Spear, F. S., Rudnick, R. L. & McDonough, W. F., 2001. Monazite-xenotime-garnet equilibrium in metapelites and a new monazite-garnet thermometer. *Journal of Petrology*, 42: 2083–2107.

Rasmussen, B., 2005. Radiometric dating of sedimentary rocks: The application of diagenetic xenotime geochronology. *Earth-Science Reviews*, 68: 197–243.

Rasmussen, B., Fletcher, I. R., Muhling, J. R. & Wilde, S. A., 2010. In situ U-Th-Pb geochronology of monazite and xenotime from the Jack Hills belt: Implications for the age of deposition and metamorphism of Hadean zircons. *Precambrian Research*, 180: 26–46.

Ruiz-Agudo, E., Putnis, C. V. & Putnis, A., 2014. Coupled dissolution and precipitation at mineral-fluid interfaces. *Chemical Geology*, 383: 132–146.

Ruschel, K., Nasdala, L., Kronz, A., Hanchar, J. M., Többens, D. M., Škoda, R., Finger, F. & Möller, A., 2012. A Raman spectroscopic study on the structural disorder of monazite-(Ce). *Mineralogy and Petrology*, 105: 41–55.

Sarma, D. S., Fletcher, I. R., Rasmussen, B., McNaughton, N. J., Mohan, M. R. & Groves, D. I., 2011. Archaean gold mineralization synchronous with late cratonization of the Western Dharwar Craton, India: 2.52 Ga U-Pb ages of hydrothermal monazite and xenotime in gold deposits. *Mineralium Deposita*, 46: 273–288.

Seydoux-Guillaume, A. M., Deschanels, X., Baumier, C., Neumeier, S., Weber, W. J. & Peuget, S., 2018. Why natural monazite never becomes amorphous: Experimental evidence for alpha self-healing. *American Mineralogist*, 103: 824–827.

Seydoux-Guillaume, A. M., Montel, J. M., Bingen, B., Bosse, V., De Parseval, P., Paquette, J., Janots, E. & Wirth, R., 2012. Low-temperature alteration of monazite: Fluid mediated coupled dissolution-precipitation, irradiation damage, and disturbance of the U-Pb and Th-Pb chronometers. *Chemical Geology*, 330–331: 140–158.

Seydoux-Guillaume, A. M., Paquette, J. L., Wiedenbeck, M., Montel, J. M. & Heinrich, W., 2002a. Experimental resetting of the U-Th-Pb systems in monazite. *Chemical Geology*, 191: 165–181.

Seydoux-Guillaume, A. M., Wirth, R., Heinrich, W. & Montel, J. M., 2002b. Experimental determination of Thorium partitioning between monazite and xenotime using analytical electron microscopy and X-ray diffraction Rietveld analysis. *European Journal of Mineralogy*, 14: 869–878.

Seydoux-Guillaume, A. M., Wirth, R., Nasdala, L., Gottschalk, M., Montel, J. M. & Heinrich, W., 2002c. An XRD, TEM and Raman study of experimentally annealed natural monazite. *Physics and Chemistry of Minerals*, 29: 240–253.

Silva, E. N., Ayala, A. P., Guedes, I., Paschoal, C. W. A., Moreira, R. L., Loong, C. K. & Boatner, L. A., 2006. Vibrational spectra of monazite-type rare-earth orthophosphates. *Optical materials*, 29: 224–230.

Spear, F. S. & Pyle, J. M., 2002. Apatite, monazite, and xenotime in metamorphic rocks. In: Kohn, M. J., Rakovan, J. & Hughes, J. M. (eds), *Phosphates: Geochemical, Geobiological, and Materials Importance*. *Reviews in Mineralogy and Geochemistry*, 48: 293–335.

Tramm, F., Wirth, R., Budzyń, B., Sláma, J. & Schreiber, A., 2021. LA-ICP-MS and TEM constraints on the magmatic and post-magmatic processes recorded by the zircon-xenotime intergrowth in pegmatite (Piława Górna, Góry Sowie Block, SW Poland). *Lithos*, 404–405: 106480.

Urusov, V. S., Grechanovsky, A. E. & Eremin, N. N., 2012. Radiation resistance of the xenotime YPO_4 from the computer simulation data. *Glass Physics and Chemistry*, 38: 55–62.

Vallini, D. A., Rasmussen, B., Krapež, B., Fletcher, I. R. & McNaughton, N. J., 2005. Microtextures, geochemistry and geochronology of authigenic xenotime: Constraining the cementation history of a Palaeoproterozoic metasedimentary sequence. *Sedimentology*, 52: 101–122.

van Achterbergh, E., Ryan, C. G., Jackson, S. E. & Griffin, W. L., 2001. Data reduction software for LA-ICPMS: Appendix. In: Sylvester P. J. (ed.), *Laser Ablation ICP–MS in the Earth Sciences: Current Practices and Outstanding Issues. Mineralogical Association of Canada, Short Course Series*, 29: 239–243.

Vielreicher, N. M., Groves, D. I., Fletcher, I. R., McNaughton, N. J. & Rasmussen, B., 2003. Hydrothermal Monazite and Xenotime Geochronology: A New Direction for Precise Dating of Orogenic Gold Mineralization. *SEG Discovery*, 53: 1–16.

Williams, M. L., Jercinovic, M. J., Harlov, D. E., Budzyń, B. & Hetherington, C. J., 2011. Resetting monazite ages during fluid-related alteration. *Chemical Geology*, 283: 218–225.

Williams, M. L., Jercinovic, M. J. & Hetherington, C. J., 2007. Microprobe monazite geochronology: Understanding geologic processes by integrating composition and chronology. *Annual Review of Earth and Planetary Sciences*, 35: 137–175.

Williams, M. L., Jercinovic, M. J., Mahan, K. H. & Dumond, G., 2017. Electron microprobe petrochronology. In: Kohn, M. J., Engi, M. & Lanari, P. (eds), *Petrochronology: Methods and Applications*. *Reviews in Mineralogy and Geochemistry*, 83: 153–182.

Wyckoff, R. W. G., 1965. *Crystal Structures, 2nd Edition, Vol. III*. Interscience Publishers, NY, London, Sydney, viii+981 pp.